12

NRL Report 8131

High-Resolution Radar Scattering Characteristics of a Disturbed Sea Surface and Floating Debris

B. L. Lewis, J. P. Hansen, I. D. Olin,
and V. Cavaleri

Target Characteristics Branch
Radar Division

July 29, 1977

NAVAL RESEARCH LABORATORY
Washington, D.C.

Approved for public release; distribution unlimited.

SECURITY CLASSIFICATION OF THIS PAGE (When Data Entered)

REPORT DOCUMENTATION PAGE

READ INSTRUCTIONS BEFORE COMPLETING FORM

1. ~~REPORT NUMBER~~ (14) NRL ~~Report~~ 8131	2. GOVT ACCESSION NO.	3. RECIPIENT'S CATALOG NUMBER
4. TITLE (and Subtitle) (6) HIGH-RESOLUTION RADAR SCATTERING CHARACTERISTICS OF A DISTURBED SEA SURFACE AND FLOATING DEBRIS.		5. ~~TYPE OF REPORT &~~ PERIOD COVERED (9) Interim report, ~~on a~~ continuing NRL problem
		6. PERFORMING ORG. REPORT NUMBER
7. AUTHOR(s) (10) Bernard L. Lewis, James P. Hansen, Irwin D. Olin and Vincent Cavaleri		8. CONTRACT OR GRANT NUMBER(s)
9. PERFORMING ORGANIZATION NAME AND ADDRESS Naval Research Laboratory Washington, D.C. 20375 (11) 29 Jul 77		10. PROGRAM ELEMENT, PROJECT, TASK AREA & WORK UNIT NUMBERS NRL Problem R12-03 Project SF12-141-41B
11. CONTROLLING OFFICE NAME AND ADDRESS Naval Sea Systems Command Washington, D.C. 20362		12. REPORT DATE July 29, 1977
		13. NUMBER OF PAGES 46
14. MONITORING AGENCY NAME & ADDRESS(if different from Controlling Office) (12) 47p.		15. SECURITY CLASS. (of this report) Unclassified
		15a. DECLASSIFICATION/DOWNGRADING SCHEDULE

16. DISTRIBUTION STATEMENT (of this Report)

Approved for public release; distribution unlimited.

(16) F12141

D D C

B

17. DISTRIBUTION STATEMENT (of the abstract entered in Block 20, if different from Report)

(17) SF12141418

18. SUPPLEMENTARY NOTES

19. KEY WORDS (Continue on reverse side if necessary and identify by block number)

High-resolution radar
Radar
Sea scatter
Sea spikes
Target detection

20. ABSTRACT (Continue on reverse side if necessary and identify by block number)

A study was made of high-resolution radar returns from a disturbed sea surface and from rigid debris floating on such a surface. The goal was to determine if there are differences between the scatter from the sea and that from debris that would permit sea return to be suppressed and debris return to be detected. The study involved both theoretical and experimental efforts. Measurement revealed that sea return was relatively improbable in any given resolution cell and that when it did occur it lasted only a second or two. Also, such return

(Continued)

DD FORM 1 JAN 73 1473 EDITION OF 1 NOV 65 IS OBSOLETE
S/N 0102-LF-014-6601

SECURITY CLASSIFICATION OF THIS PAGE (When Data Entered)

251 950

1B

20. Abstract (Continued)

was always heavily amplitude modulated with modulation frequencies much higher than those on debris echoes. These findings were explained theoretically and used in developing a debris-avoidance radar concept for high-speed ships.

CONTENTS

SUMMARY

This report describes work done in developing a concept for the design of an effective debris-avoidance radar for use on high-speed ships. The work included experiments to measure the echoing characteristics of the disturbed sea surface and of rigid debris floating on the surface in various sea states. The goal was to find a way to suppress sea return and detect debris.

A dual-frequency X-band radar with selectable polarization and variable pulse length (0.5 to 0.02 ns) was developed for this purpose. Measurements were made near shore in the Chesapeake Bay and in deep water of Boca Raton, Florida.

The experimental program revealed significant differences between echoes from the sea surface and those from rigid floating debris.

Sea return was found to be very improbable in any given range resolution cell for pulse lengths of 100 ns or less. When large sea returns (often called sea spikes) were received in any resolution cell, they lasted for less than 2 s and were not repeated in that cell for 15 to 100 s. In addition, all X-band sea return in any sea state was found to be amplitude modulated with a high percentage of modulation at frequencies on the order of 50 to 170 Hz. In any sea state, the probability of sea return in any given resolution cell was found to be much higher with vertical polarization than with horizontal polarization.

Returns from rigid floating debris were found to have much lower amplitude modulation frequencies than sea return in any sea state tested and with any polarization employed. In addition, the probability of a return from rigid debris was much higher than the probability of sea return in the range cell occupied by the debris for pulse lengths less than 100 ns.

A theoretical model explaining the sea return characteristics was developed. It demonstrates that conventional radar could not be used to detect debris because it would suffer an unacceptable false alarm rate due to the random appearance of sea spikes.

The difference in the modulation frequencies of sea and debris returns was used in developing a detector that eliminates sea spikes and detects debris return. This detector requires the radar to dwell on any resolution cell for about 20 ms. Thus, the proposed radar employs multiple fixed beams covering an angular sector in front of the ship.

HIGH-RESOLUTION RADAR SCATTERING CHARACTERISTICS OF A DISTURBED SEA SURFACE AND FLOATING DEBRIS

INTRODUCTION

This report will describe work done in developing a concept for an effective debris-avoidance radar for high-speed ships. The work included both experimental and theoretical efforts and resulted in a better understanding of sea scatter phenomena and a new concept for debris detection radar design.

The goal of this study was to find a technique for designing a radar that would detect debris floating on a disturbed sea surface. The problem was to differentiate between echoes from debris and those from the disturbed sea surface.

The approach to the problem was to measure the characteristics of sea return as a function of polarization, carrier frequency, range resolution, angle resolution, and time. The same measurements were then made on rigid debris floating on the water, and comparisons were made to determine whether there were any characteristics that would distinguish one from the other.

INSTRUMENTATION

A schematic of the radar developed to study debris and sea return is shown in Fig. 1. Two continuous-wave (CW) signal generators are used as carrier sources. One generator is tuned to 8.6 GHz, and the other to 9.2 GHz. The outputs of these two generators are added in a hybrid and amplified in a traveling wave tube (TWT) chain; they then excite the input of a normally open diode switch. This switch is closed for the duration of a pulse from a timing generator. The minimum usable pulse length is 20 ns, and the maximum pulse length is limited by the pulse repetition period of the timing generator, which is variable from 0.02-1 ms. The output of the switch passes through a circulator, then through a polarization selector switch, and is radiated from an antenna as either a vertically or horizontally polarized wave. The antenna is a parabolic reflector either 1 or 2.67 m in diameter with orthogonally linearly polarized feeds separately connected to the polarization switch.

Radar echoes that enter the antenna pass through the polarization switch and enter the radar receiver through the circulator and a diode switch that is closed by a receiver gate pulse from the timing generator. The output from this switch passes through a calibrated variable attenuator and is amplified by a low-noise TWT chain. The output of the TWT chain enters port A of a four-port circulator and couples to a bandpass filter that is 200-MHz-wide, tuned to 8.6 GHz, and attached to port B of the circulator.

Manuscript submitted May 18, 1977.

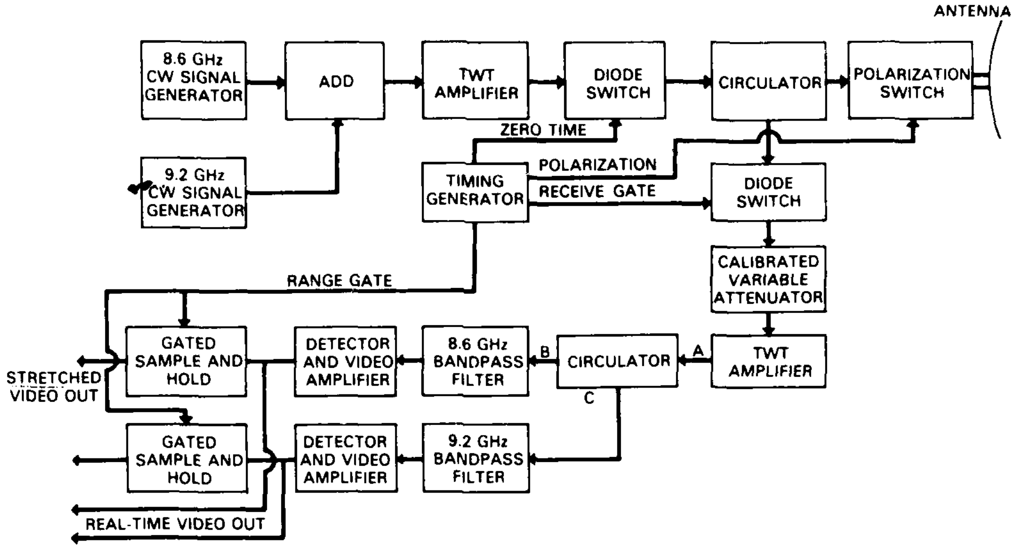

Fig. 1 — Instrumentation radar

The 8.6-GHz signal passes through this filter, and the 9.2-GHz signal reflects back into port B of the circulator. The 9.2-GHz signal exits from port C of the circulator and passes through a bandpass filter 200-MHz-wide and tuned to 9.2 GHz. The outputs of these two filters are rectified in separate detectors and amplified in separate wide-band video amplifiers. The outputs of these amplifiers are displayed as real-time video on a two-channel oscilloscope and are also used as inputs to two range-gated sample-and-hold circuits. The gated stretched outputs of the sample-and-hold circuits are displayed as time functions on a two-channel oscilloscope and are also recorded on a two-channel magnetic tape recorder.

Figure 2 is a schematic of the data recording complex. A television camera with a zoom lens was mounted on the radar antenna with its field of view centered on the radar field of view. Two other television cameras were used to record the real-time video and the range-gated time functions displayed on two-channel oscilloscopes. Split-screen techniques were used to record the output of all three television cameras on the same television recorder. This ensured time synchronization of the radar data and the optical picture of the sea surface that produced the radar echoes.

CALIBRATION

The system was calibrated using a corner reflector with a known equivalent scattering cross section of $\sigma = 24\ \text{m}^2$ (Fig. 3). The variable attenuator at the input to the receiver was adjusted so that both the real-time video and the gated stretched video were at the upper end of the linear range of the system.

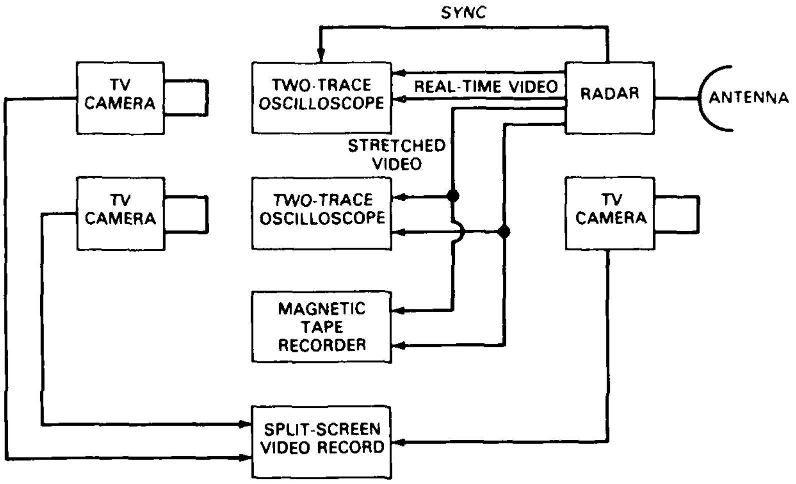

Fig. 2 — Recording instrumentation

In Fig. 3 the right-hand section of the picture is the view from the boresight camera. The inset at the bottom left is the real-time video and the range gage. The lower trace is 8.6 GHz, the middle trace is 9.2 GHz, and the upper trace is the approximate range gate position. The sweep speed for the real-time video was 50 ns/cm, or 500 ns per sweep. The inset at the top left is the gated stretched video with 9.2-GHz top and 8.6-GHz bottom trace. The sweep speed of these traces was 20 ms/cm (0.2 s per sweep). The circular dark spot on the boresight picture is the region filled by the radar beam at ranges long enough to minimize the parallax between the TV camera and the antenna. The dotted lines in this dark spot are the region covered by the 20-ns range gate when the beam strikes the water at a 4.6° grazing angle viewing the disturbed sea surface.

In these measurements, the radar pulse repetition frequency was 50 kHz.

EXPERIMENTAL RESULTS

The first measurements of sea return were made at the Chesapeake Bay with the 1-m diameter radar antenna, 4 m above the mean water level. The radar beamwidth with this antenna was 2.6°, and the center of the beam impinged on the water at a distance of 50 m. These values yielded a 2-m cross-range resolution cell at the center of the beam and a grazing angle of 4.6°. The radar pulse length and range gate were 20 ns long, yielding a range resolution of 3.33 m.

Figure 4 typifies data obtained with vertical polarization and with 1- to 1.3-m waves. The individual pictures were taken sequentially in time with approximately 0.3 s between pictures. This time interval corresponded to the time between sweeps of the oscilloscope

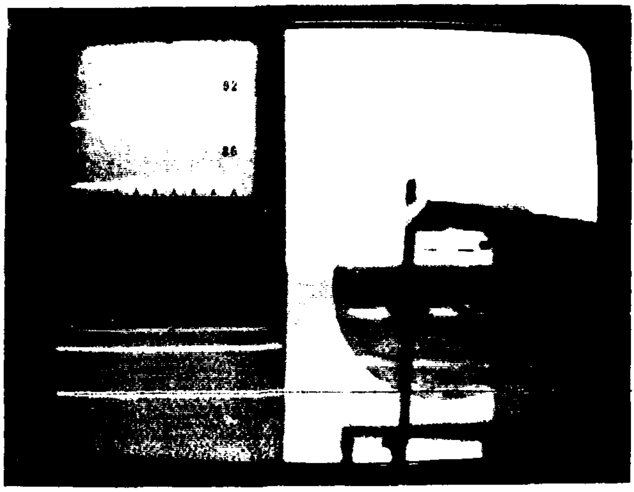

(a) 50-dB attenuation in receiver

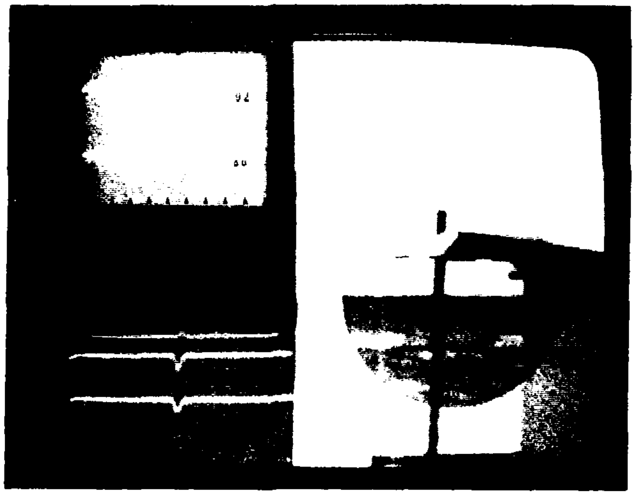

(b) 15-dB attenuation in receiver

Fig. 3 — Calibration via corner reflector ($\sigma = 24\ \mathrm{m}^2$)

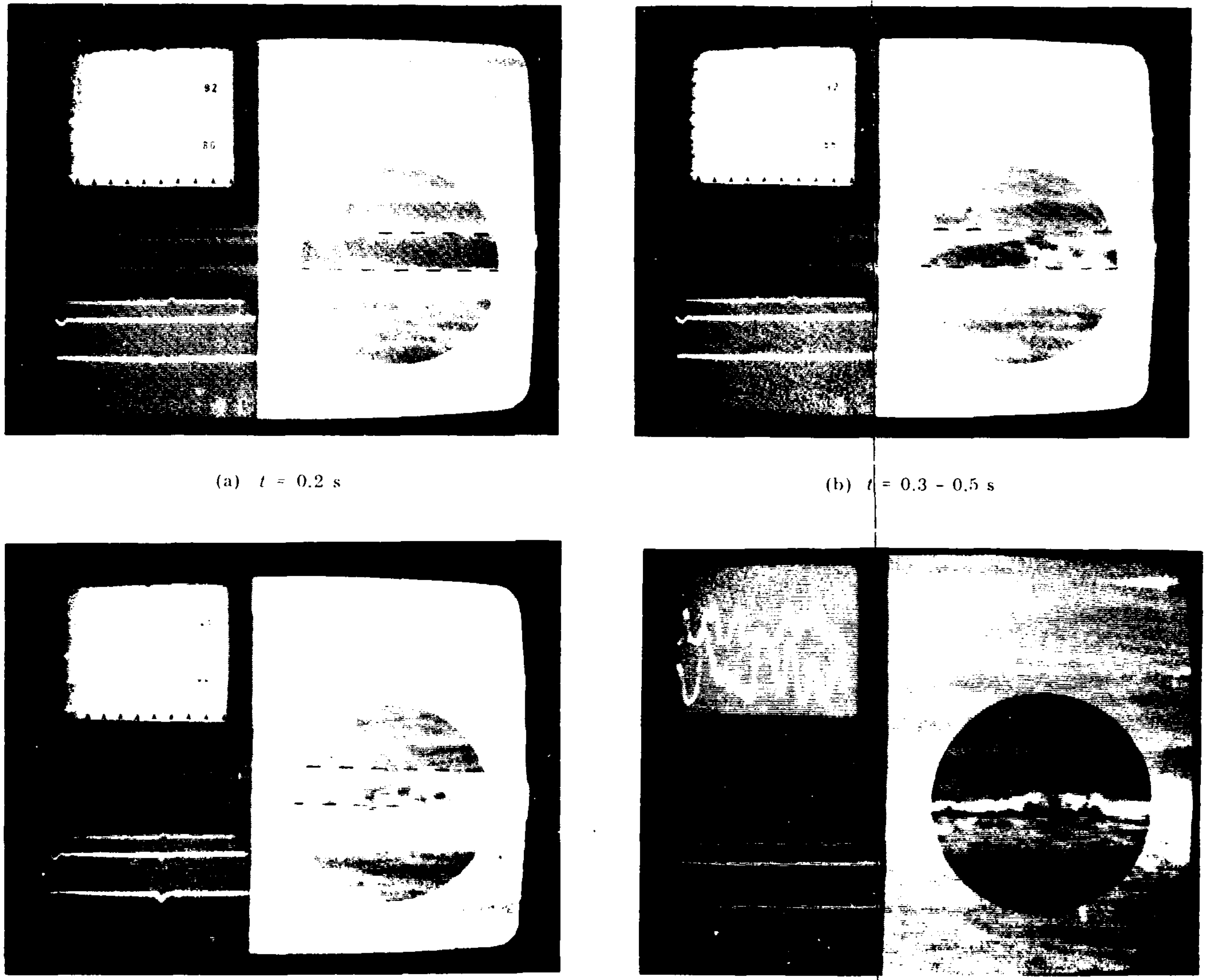

(a) $t = 0.2$ s

(b) $t = 0.3 - 0.5$ s

(c) $t = 0.6$ to 0.8 s

(d) $t = 0.9$ to 1.1 s

Fig. 4 — Sea return data obtained with vertical polarization (6-dB attenuation in receiver

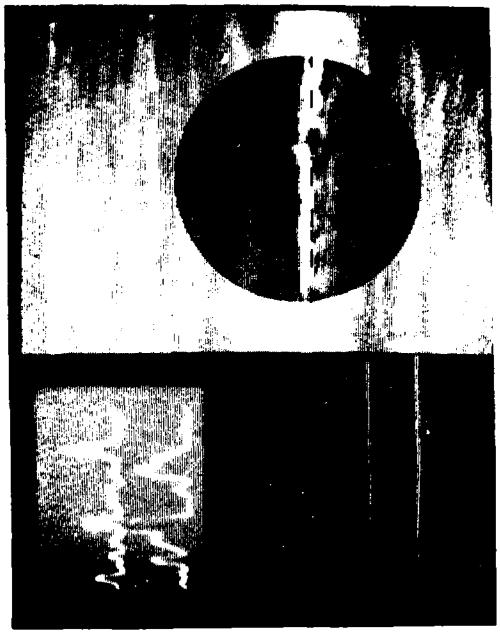

(e) t = 1.2 to 1.4 s

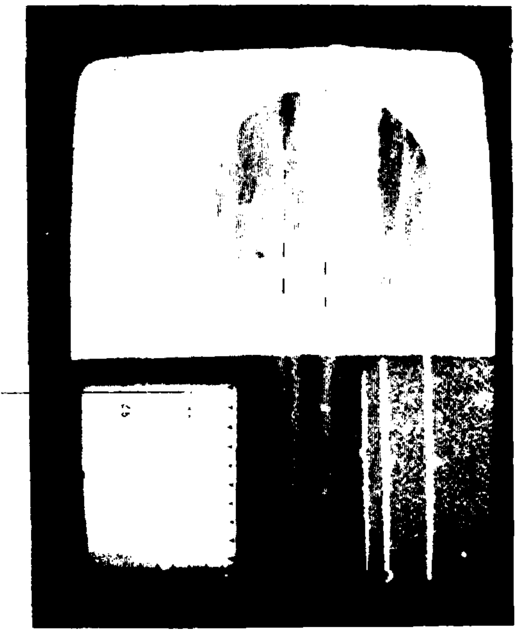

(f) t = 1.5 to 1.7 s

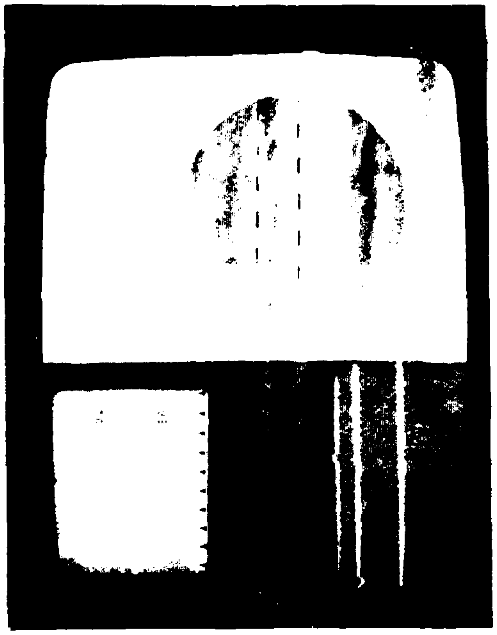

(g) t = 1.8 to 2.0 s

Fig. 4 (Continued)

portraying the gated stretched video. It should be noted that the real-time video displayed in these pictures corresponded to the last displayed stretched video only when the photos were taken before the stretched video sweep ended. In all data, the oscilloscopes sweep from left to right in time.

Figure 4a is the start of the sequence and reveals 8.6-GHz returns (real-time video) from two waves, one in front of and the other behind the range gate. The latter appears to originate from the sharp peak or crest of the second wave, and the former corresponds to the whitecap on top of the first wave. No returns are evident on 9.2 GHz.

Figure 4b portrays the sea surface 0.3 s later, with a large wave in the range gate but no real time video returns evident on either frequency. The stretched video, however, shows evidence of some small returns on both frequencies between pictures.

Figure 4c was taken 0.3 s after 4b and shows whitecaps at the two sides of the wave in the range gate, a real time video return at 8.6 GHz (note the pulse fill-in), and data on both frequencies in the stretched video display. The largest peaks in the stretched video correspond to an equivalent scattering cross section σ on the order of 1.6 m^2 in the resolution cell. The stretched video also shows that the return is heavily amplitude modulated, with nearly 100% amplitude changes in times on the order of 10 ms.

Figure 4d, taken 0.3 s after Fig. 4c, shows a whitecap filling the azimuth resolution cell as the whole wave breaks. Returns are evident on both frequencies in the real-time data, and large returns are evident in the stretched video traces. The width of the visible whitecap in range is on the order of 1 m, and the peak equivalent scattering cross sections evident from the stretched video are in excess of 4 m^2 at 9.2 GHz and 7 m^2 at 8.6 GHz. Note that the two frequency-stretched video time functions appear to be uncorrelated, as one would expect, due to the large frequency difference (600 MHz).

Figure 4e, taken 0.3 s after Fig. 4d, shows the whitecap moved toward the short range side of the range resolution cell. The stretched video shows an extremely large return on 8.6 GHz that actually went off scale and saturated. This required a σ in excess of 10 m^2.

The next picture in the sequence (4f) shows large real-time video almost out of the range gate, and Fig. 4g completes the sequence of the wave moving through the range gate.

Figure 5 is another typical vertical polarization sequence of a whitecap forming and moving out of the range gate. Note that the wave traveled about 1.33 m in 1.2 s and that the size and shape of the broken water region were constantly changing. The largest σ values in this sequence were on the order of 7 m^2. Figure 6 is a wave sequence taken

Figure 6 is a wave sequence taken with the radar polarized horizontally. In these data, the calibrated attenuator was varied to increase the receiver sensitivity by 5 dB. The time intervals between pictures in the sequence were 0.3 s, as in the vertically polarized case, and all trace speeds were maintained.

Figure 6a shows a whitecap forming on a wave at the outer end of the range resolution cell. *Note the optical image of the whitecap in the water in front of the whitecap.*

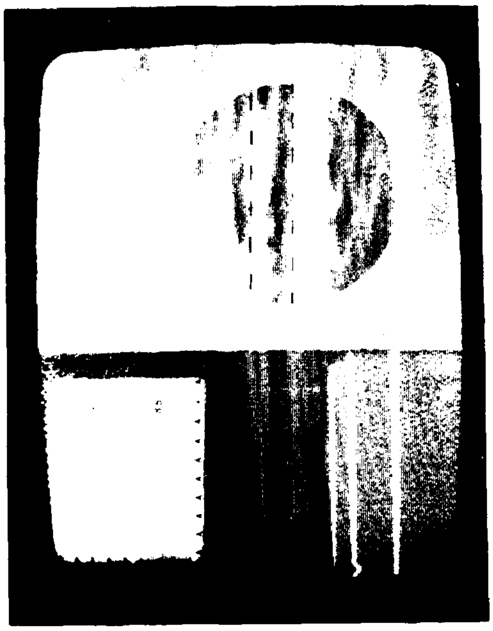

(a) t = 0 to 0.2 s

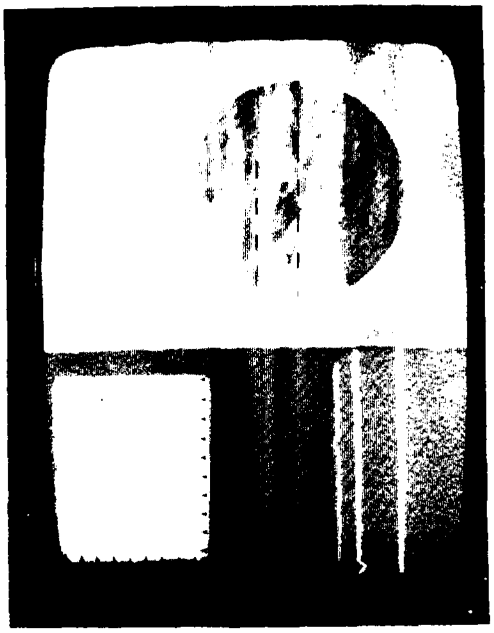

(b) t = 0.3 to 0.5 s

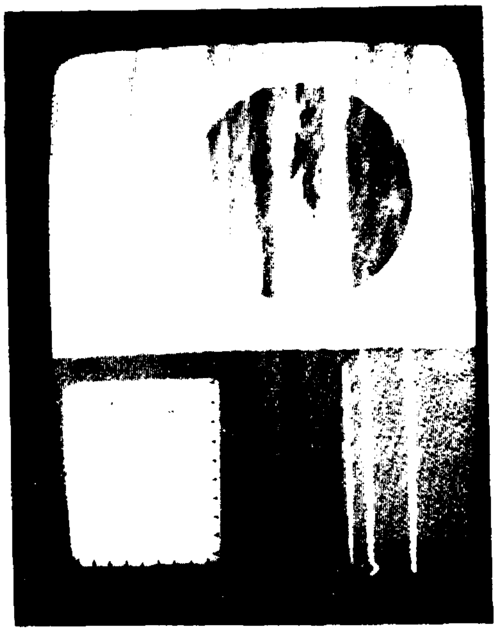

(c) t = 0.6 to 0.8 s

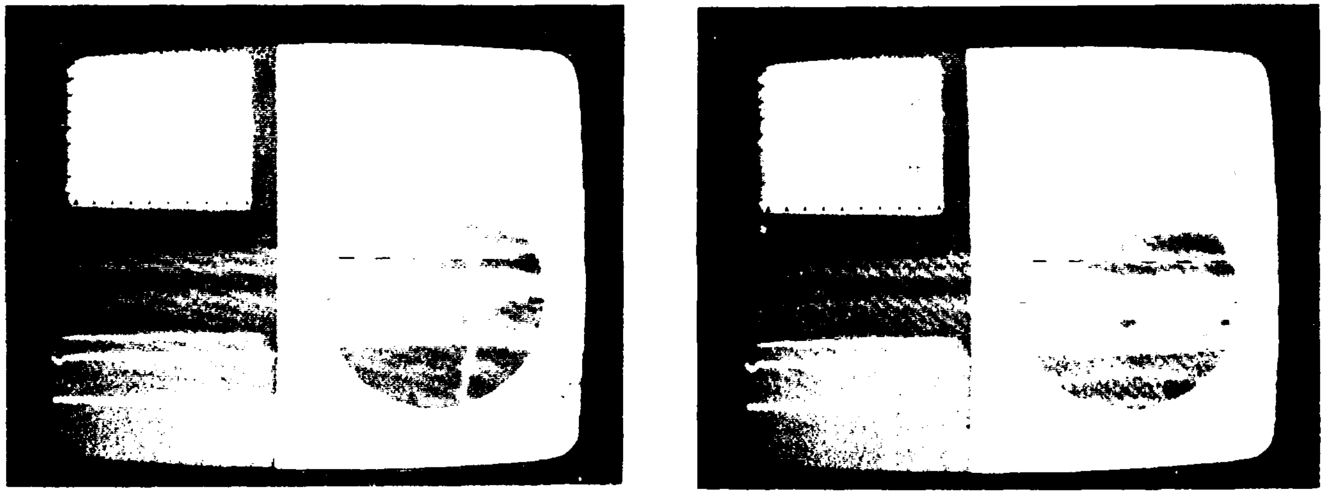

(d) t = 0.9 to 1.1 s   (e) t = 1.2 to 1.4 s

Fig. 5 — Sea return data obtained with vertical polarization (6-dB attenuation in receiver)

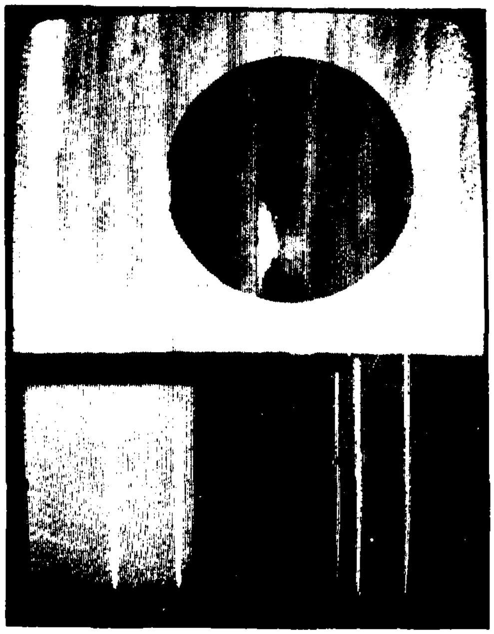

(a) t = 0 to 0.2 s

(b) t = 0.3 to 0.5 s

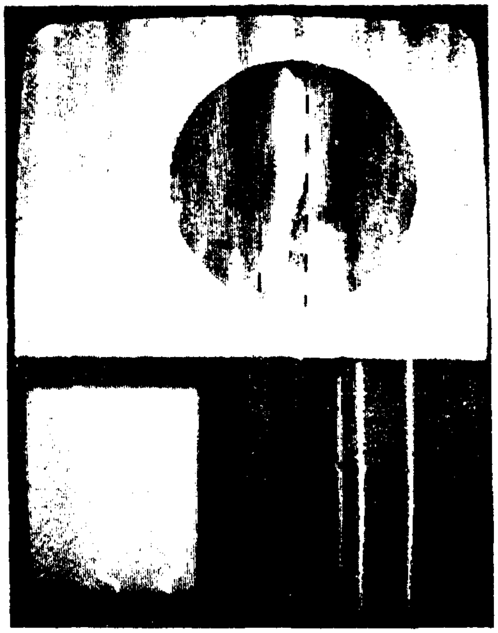

(c) t = 0.6 to 0.8 s

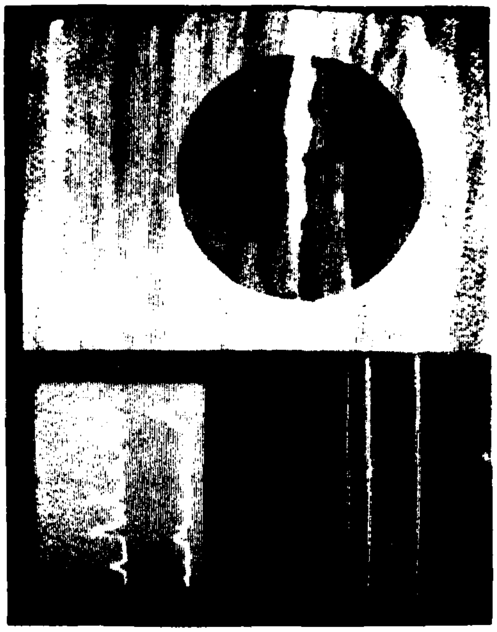

(d) t = 0.9 to 1.1 s

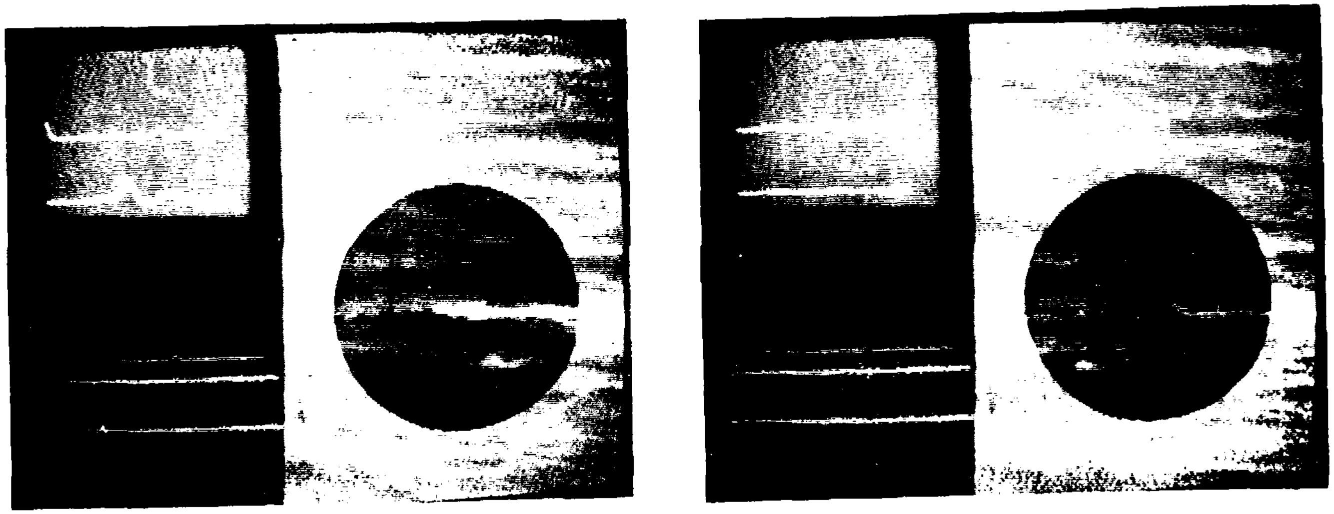

(e) t = 1.2 to 1.4 s

(f) t = 1.5 to 1.7 s

Fig. 6 — Sea return data obtained with horizontal polarization (1-dB attenuation in receiver)

This optical imaging was noted many times in the measurement program and will be shown to be significant in later sections of this report. Real-time video is evident, but the stretched video trace had ended prior to the video occurrence and shows no data.

Figure 6b shows the whitecap greatly increased in size and indications of returns on the gated stretched video traces. The peaks in those traces correspond to σ values of 0.2 m^2.

Figure 6c shows larger echoes on the stretched video traces, with peak σ values of about 1 m^2. Note the characteristic high-frequency, large-percentage amplitude modulation on the echo as a function of time.

Figure 6d shows both real-time video and previous echoes from σ values on the order of 1.5 m^2 peak. Figures 6e and 6f complete the sequence.

Figure 7 is another typical sequence with horizontal polarization. Figure 7a starts the sequence with no visible returns but with a large wave in the resolution cell.

Figure 7b shows the wave starting to break and evidence of radar echoes in the gated stretched video. The peak echoes on 9.2 GHz were from σ values on the order of 1 m^2, and those on 8.6 GHz were on the order of 0.5 m^2.

Figure 7c shows the wave break expanding across the azimuth resolution cell. Real-time video is evident, and rapidly modulated returns are evident in the gated stretched video. The σ values in this picture were in excess of 1.5 m^2 at 9.2 GHz and 0.5 m^2 at 8.6 GHz.

Figure 7d shows evidence of a very large return on 8.6 GHz ($\sigma \approx 2.5$ m^2), and the wave is broken over most of the azimuth resolution cell.

Figure 8 shows the radar return from a semisubmerged platform on both horizontal (Fig. 8a) and vertical (Fig. 8b) polarization. Note that the echo is modulated as the water rises and falls. Note also that this modulation is very low in frequency compared to that characteristic of echoes from breaking waves.

DEEP WATER DATA

Sea return measurements were also made at Boca Raton, Florida, in deep water. In these measurements, the 2.67-m-diameter antenna was employed with a 1° beamwidth. The antenna was mounted on top of a building 13 m above mean sea level, and the center of the beam intercepted the water at a distance of 530 m. This produced a grazing angle of about 1.4°. The boresight television camera field of view was narrowed to permit it to cover the radar beam in azimuth (1°) on the split-screen display, and it provided a 2° vertical field of view.

The 530-m range and 1° beamwidth produced an azimuth resolution of about 10 m, and the 20-ns pulse yielded a range resolution of 3.33 m.

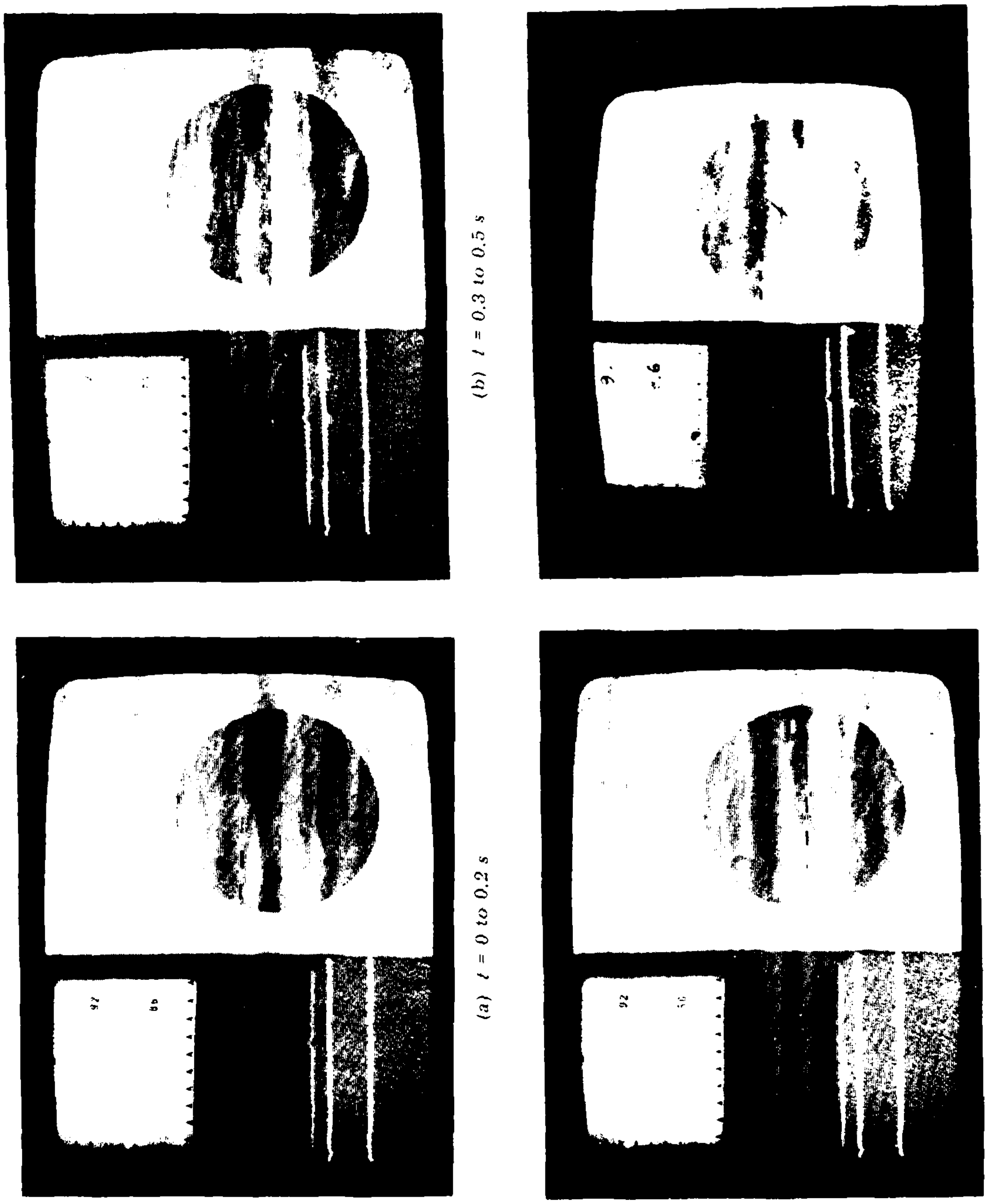

(a) t = 0 to 0.2 s

(b) t = 0.3 to 0.5 s

(c) t = 0.6 to 0.8 s

(d) t = 0.9 to 1.1 s

Fig. 7 — Sea return data obtained with horizontal polarization (1-dB attenuation in receiver)

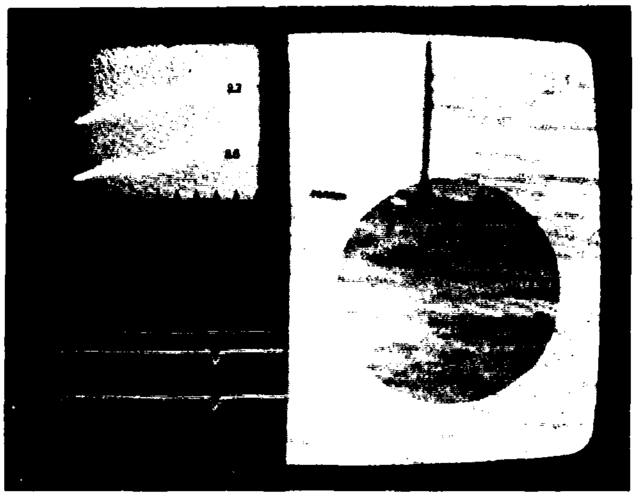

(a) horizontal polarization

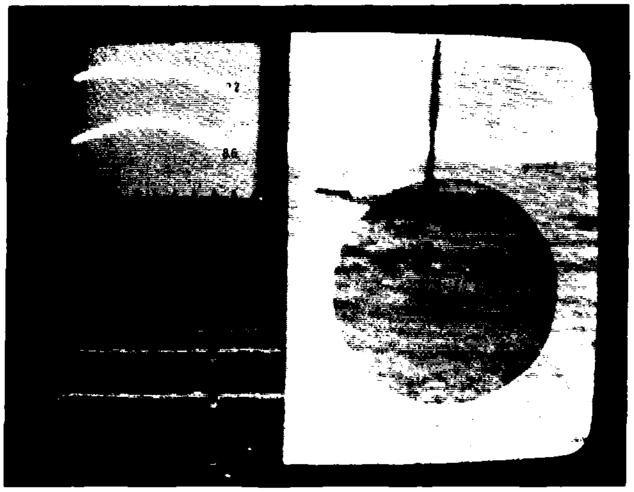

(b) vertical polarization

Fig. 8 — Return from partially submerged platform
(1-dB attenuation in receiver)

Whitecap data obtained from this site with 1- to 1.3-m waves were very similar to data obtained at Chesapeake Beach. However, an opportunity occurred to observe whitecaps from waves traveling across the field of view. Data from these waves revealed much higher frequency amplitude modulation than those from waves breaking toward the radar. Autocorrelation times on the order of 3 ms were observed. Figure 9 is characteristic of the returns for vertical and horizontal polarization. (The triangular marker on the side of the boresight picture marks the range gate position.)

The increased frequency of the amplitude modulation can be explained by the increased rate of growth of the whitecap in range due to the angle between the wavefront and the line of sight. Note that the growth rate of the Chesapeake Beach whitecaps (Fig. 6) was much higher along the water wavefront than normal to the wavefront. Differences of 4 to 1 were common.

Data were also obtained on small unbreaking waves at Boca Raton, Florida. These waves ranged from 0.15 to 0.3 m in height. Analysis of this data has not been completed at this time. However, several obvious facts were noted. These were as follows:

1. The echoes (Fig. 10) had the same temporal and spatial characteristics as those from whitecaps but were much smaller in magnitude. They had autocorrelation times of 10 ms or less and were widely separated in range (relatively improbable in any given range resolution cell).

2. Echoes on horizontal polarization were less probable than on vertical polarization but were higher in amplitude when received. The latter effect was attributed to the fact that the angle of incidence on the waves was near Brewster's angle for vertically polarized radiation.

3. The lifetime of any return was on the order of 1 s or less.

MEDIAN EQUIVALENT SCATTERING CROSS SECTION OF WHITECAPS

The large equivalent scattering cross section of whitecaps at small radar depression angles can be explained theoretically by assuming them to be very rough surfaces at the wavelength of interest (3 cm). Such rough surfaces scatter incident radiation in all directions in the upper half space.

The grazing angle of the radiation on the whitecap can be approximated by the sum of the radar depression angle and half the slope of the wave when it breaks (30°). Thus, for small depression angles, the power intercept area of the whitecap can be taken to be

$$A_S = A \sin 15^\circ = A/4, \qquad (1)$$

where A is the actual area of the visible whitecap.

With this power intercept area, the equivalent scattering cross section is

$$\sigma = A_S \, G_S = A G_S / 4, \tag{2}$$

where G_S is the gain of the scatterer in the direction of the radar receiver. G_S in this case will be determined by the roughness of the whitecap, by the fact that energy can scatter only into the upper half space, and by the fact that an image of the whitecap will form in the surrounding unbroken water, i.e.,

$$G_S = G_R \, G_{HS} \, G_{TI} \tag{3}$$

where G_R is the roughness factor, G_{HS} is the half-space factor, and G_{TI} is the target-image factor.

For very rough surfaces $G_R \approx 1$, $G_{HS} = 2$, and $G_{TI} = 2$, since the image of the whitecap can have the same power intercept area as the whitecap. With these values, Eq. (2) becomes

$$\sigma = A_S. \tag{4}$$

It should be noted at this point that the σ, given by Eq. (4), is the mean value. Since the target and its image are illuminated by coherent radiation, they can interfere constructively and destructively. In addition, the coherent scatter from the different portions of the rough surface can interfere constructively or destructively. In fact, the whitecap's height above mean sea level and its size and structure will change with time. This will cause severe amplitude modulation of σ with time, as observed in the data obtained in sea return measurements.

The measurement program revealed that Eq. (4) is useful and reasonably accurate. Dividing this equation by A to obtain σ_0 yields $\sigma_0 = 1 \text{ m}^2/\text{m}^2$. This is on the order of 35 dB greater than the σ_0 quoted in standard tables for sea scatter in low-resolution radars for sea states 3 and 4 and 3° grazing angles [1]. The difference can be justified by the large ratio of sea surface not covered by whitecaps to that covered by white caps.

Applying Eq. (4) to the data in Fig. 4d, where A_S was noted to be 1 m deep in range by 2 m in azimuth, would yield an average $\sigma \approx 2 \text{ m}^2$. This is in reasonable agreement with the data, considering the statistics involved.

MULTIPATH EFFECTS

Interference between the echo from the whitecap and its image can produce a relatively slow modulation on the composite return as the object and image spacing vary with time. As previously noted, images have been observed at optical frequencies and

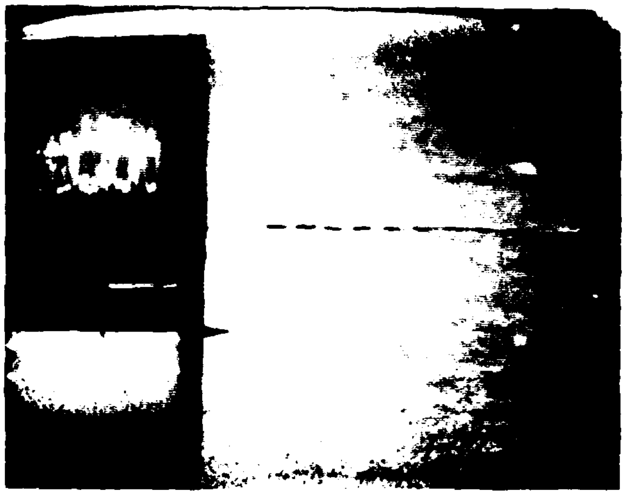

(a) vertical polarization

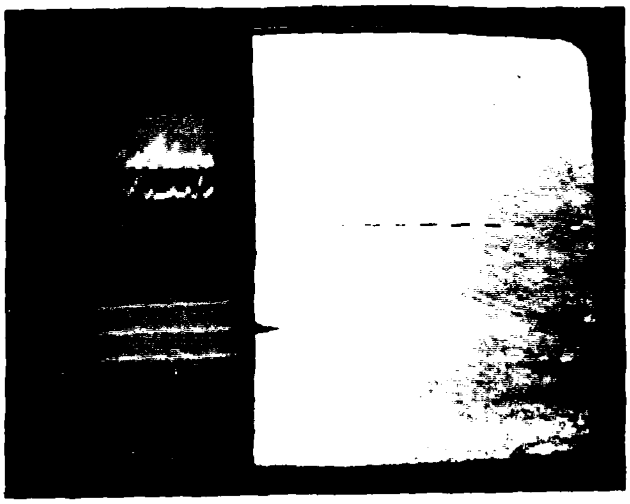

(b) horizontal polarization

Fig. 9 — Returns obtained in deep water, 20 ms/cm sweep; stretched video

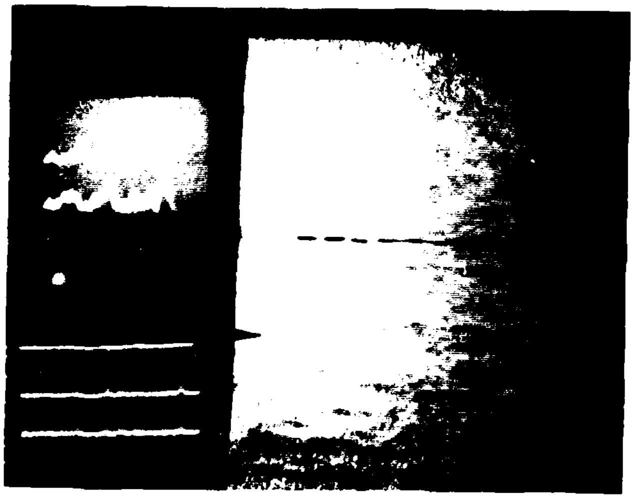

(a) vertical polarization

(b) horizontal polarization

Fig. 10 — Returns from small waves in deep water

would be even more likely at microwave frequencies. Whitecaps appear frequently at sea state 3, for which the wave height and period are about 1.25 m and 4 s, respectively. At a wavelength of 3.3 cm (corresponding to 9.1 GHz), the vertical lobing pattern width ($\theta = \sin^{-1} \lambda/2H$) is about 0.8°. For the CBD tests the grazing angle was 4.6°, so that the radar antenna was located in the sixth lobe of the whitecap interference pattern. For the 4-s period, this suggests a maximum detected modulation frequency of 3 Hz. At most radar operating ranges, the grazing angle will be much less. If it is less than 0.8°, the signal variation due to multipath will be at the wave period, corresponding to a frequency of 1/4 Hz. The elevation lobing phenomenon is suggested as one reason for observed time delays that often occur between the formation of a whitecap and the reception of the sea spikes. It can also explain the relatively long time in which either the 8.6- or 9.2-GHz return is detected in the absence of the other.

POLARIZATION DEPENDENCE OF WHITECAP ECHOES

All the data taken in this study revealed that the equivalent scattering cross section of broken water (whitecaps) was on the order of 5 dB higher for vertical polarization than for horizontal polarization. This agrees with Nathanson [1]. However, this difference is not predictable on the basis of scattering from a randomly rough surface. Such a surface should scatter all polarizations equally.

A possible clue to the cause of this polarization sensitivity was obtained from echoes from sharp-topped, unbroken waves. Such echoes are much higher for vertical polarization than for horizontal polarization. The sharp top acts as an impedance discontinuity to surface currents induced by incident radiation. Such currents partially reflect from this discontinuity and radiate backward like long-wire standing wave antennas [2,3] with significant directivity and gain. An example of such augmentation of equivalent scattering cross section is evident in the variation of σ with incidence angles of radiation on a long wire.

Skolnik [4] shows such a plot for a rod 39 wavelengths long and 1/4 wavelength in diameter. This plot shows σ falling off rapidly with the departure of the grazing angle from 90°. However, σ begins to rise again at small grazing angles and peaks at about 8° to a value several orders of magnitude greater than that at larger grazing angles. This 8° angle is the position of the largest radiation lobe of such a rod when excited by a current, at the frequency of interest, inserted at one end.

This mechanism could explain the polarization sensitivity of sea scatter since the high-gain lobes make small angles with the reflected surface current and since no reflected surface currents are produced by incident radiation with the E field parallel to the sharp top of the wave. Vertically polarized radiation will induce such reflected currents on wave tops with the maximum scatter gain back in the direction of the radar (in monostatic systems), as shown in Fig. 11. Horizontally polarized radiation can induce such reflected signals, but the reflected surface currents will make big angles with the line of sight from the radar (Fig. 12) and the large high-gain long-wire lobes will miss the radar.

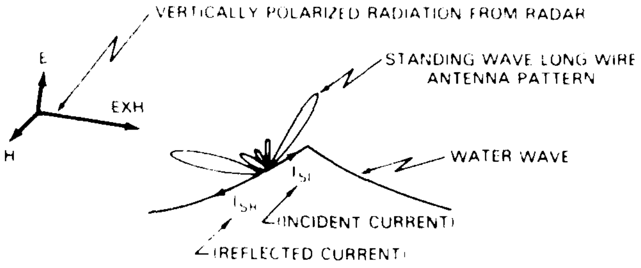

Fig. 11 — Vertically polarized scatter from water wave

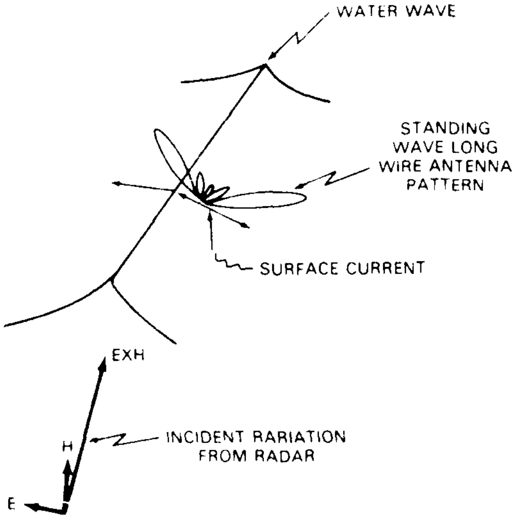

Fig. 12 — Horizontally polarized scatter from water wave

This phenomenon can be very important in the case of whitecaps, where there is an abrupt discontinuity between the unbroken water and the broken water falling down the face of the wave (Fig. 13). In this case, echoes from horizontally polarized radiation would originate mainly in the rough broken water, while those from vertically polarized radiation would originate both in front of and within the broken water.

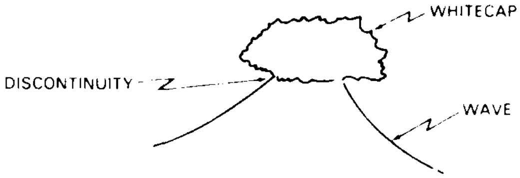

Fig. 13 — Discontinuity at whitecap-wave interface

Future work is planned to test this hypothesis using bistatic radar measurements of sea scatter.

THEORETICAL SCATTERING MODELS

Many hours of high-resolution radar sea return recordings were made in the Chesapeake Bay and in deep water off Boca Raton, Florida. In all cases, large returns were found to be associated with broken water in whitecaps; returns from unbroken water were much smaller. In all cases the returns were found to be amplitude modulated, with relatively high frequencies and high modulation indexes. If these findings are generally applicable, they provide a basis for discriminating between sea return and echoes from rigid debris floating on the water, because the latter would display much lower frequency-amplitude modulations. The general applicability of these observations would be more acceptable if theoretical analysis explained and predicted the modulation characteristics of sea return. As a consequence, a theoretical analysis was undertaken.

The approach to this analysis was to construct a series of possible models of the surface and to compare calculated scattering from these surfaces with measured data from the sea surface.

In modeling the surface, it was noted that coherent illumination at low grazing angles at a wavelength λ would define the autocorrelation length in range to be $\lambda/4$; i.e., echoes from scatterers separated in range by less than $\lambda/4$ would be correlated and would interfere constructively. It was also noted that the autocorrelation time of the X-band echoes from whitecaps was on the order of 10 ms, and that this corresponded very closely to the observed time necessary for the whitecap to grow or shrink in range length by $\lambda/4$. This growth rate was also measured by B. L. Hicks et al. [5]. As a consequence, all models employed one scatterer per $\lambda/4$ range increment, rather than a continuum of scatterers.

All models of whitecaps were based on the assumption that the whitecap started from zero size, grew in range to a finite value, then shrank back to zero. This growth or shrink rate was assumed to be on the order of $\lambda/4$ in 10 ms. These assumptions were based on hours of visual study of the sea surface via television cameras with known frame rates and thus were not completely arbitrary.

The various models constructed differed in the degree of randomness of the surface and in the ratio of internal to external autocorrelation times. The latter is the time of addition of an extra $\lambda/4$ zone, and the former is the decorrelation time of scatterers in zones already formed.

The first model of the surface to be constructed assumed that the amplitude of the reflected signal from the nth $\lambda/4$ zone added would be represented by

$$e_n = (1 - kV_n)(-1)^{n-1} \tag{5}$$

where V_n was picked from a table of random numbers uniformly distributed between 0 and 1, and k was the assumed randomness, having a value from 0 to +1. The equivalent scattering cross section of a surface composed of n zones was then defined to be

$$\sigma_n = \left(\sum_{i=1}^{n} e_i \right)^2 . \tag{6}$$

Differences in internal and external autocorrelation times were incorporated by updating (drawing new random numbers for) already formed zones when such zones were m zone additions old. For example, an $m = 1$ would imply equal internal and external autocorrelation times and was instrumented by summing new random numbers for each zone every time a new zone was added. Thus, σ_n involves different random numbers from those forming σ_{n-1} or σ_{n+1}. An $m = 5$ would imply an internal autocorrelation time five times longer than the time required for the surface to grow by one zone. Thus, new random numbers would be drawn for zones that are five zone additions old.

For all models, σ was plotted against n (the number of zones formed) for five different realizations of the surface (five different sets of random numbers) and for k values of 1, 0.50, and 0.25. In all cases n_{max} was taken to be 128, which at X-band would correspond to a whitecap 1.05 m long. In addition, the spectrum of the resultant time function was plotted by passing the function through a 128-point fast Fourier transform (FFT) program. Since only real numbers were used, the plot was extended only to 65 frequencies, because frequencies from 65 to 129 would be the mirror images of those plotted.

Figure 14 is a plot of σ vs n for $k = 0$. Note the σ variation from 0 to 1 to 0, etc., as zones are added (as would be expected). The spectrum in Fig. 14 is the result of passing the σ values through the FFT, which produced a DC term and a term at half the sampling rate.

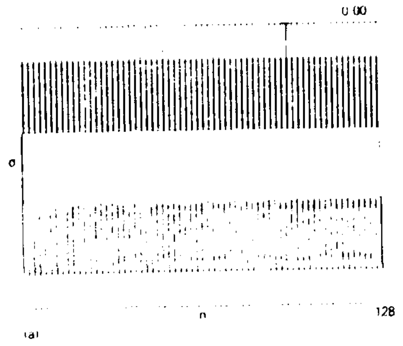

(a) σ vs n

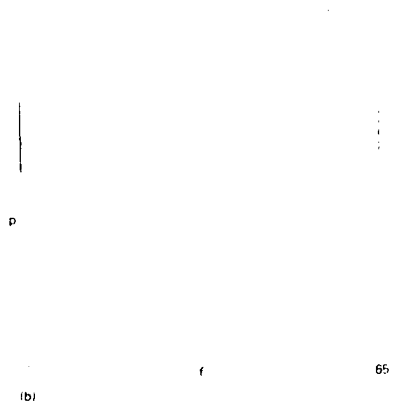

(b) power P vs frequency f

Fig. 14 — Random-amplitude model, k = 0

Figures 15a through 15e are σ and spectra plots of different realizations (different random numbers) with $k = 0.25$ and $m = 1$. In these plots, the vertical scale is fixed by the largest value encountered, and the spectra are the result of passing the amplitudes associated with the σ values through the FFT. In these spectra the amplitudes were equally likely to be positive or negative. Note that the largest peaks are on the order of eight times the value for one zone, which in this case is dominated by the coherent component and is evident at $n = 1$, 3, and 5.

Figure 15f is the average spectrum of the five realizations with $k = 0.25$ and $m = 1$.

Figures 16a through 16e are the σ and spectra plots of five different realizations of $k = 0.5$ and $m = 1$, with the vertical scale normalized to the largest peak. Note that the largest peaks have increased with respect to the average σ for one zone due to the increase in k. Again, the spectra resulted from passing the amplitude values from which the σ plot was derived through the FFT. As a consequence, the DC component is relatively small compared to the total power in the spectrum. Figure 16f is the average spectrum of the five realizations.

Figures 17a through 17e are the result of $k = 1$, i.e., a completely random surface. Note that the largest σ values are many times that for one zone and the spectrum contains many high-frequency components plus a DC term. Figure 17f is the average spectrum.

Comparison of these data with the experimental results shows good agreement, especially with $k = 1$.

Figures 18 through 20 are the results of k values of 0.25, 0.5, and 1 and an m value of 5; i.e., zone updates every five zones added. These results give longer spikes (longer autocorrelation times) than were evident in the experimental results.

The agreement of the model used for Fig. 17 with the measured data indicates that whitecaps are very rough surfaces with nearly equal internal and external autocorrelation times. The agreement also adds confidence that the water dynamics will always produce a sea return with high-percentage high-frequency amplitude modulations.

The previously discussed theoretical models employed only random amplitude. The return from each zone was assumed to come from the center of the zone. Another type of model was also developed that allowed both the amplitude and phase of zone returns to vary.

In this model, the return from the nth zone was defined as

$$e_n = (-1)^{n-1}(1-kV_{n1})\left\{\cos\left[k\left(\frac{1}{2} - V_{n2}\right)\pi\right] + j\sin\left[k\left(\frac{1}{2} - V_{n2}\right)\pi\right]\right\} , \tag{7}$$

where k is the randomness factor $0 \leqslant k \leqslant 1$ and V_{n1} and V_{n2} are two random numbers, each uniformly distributed between 0 and 1.

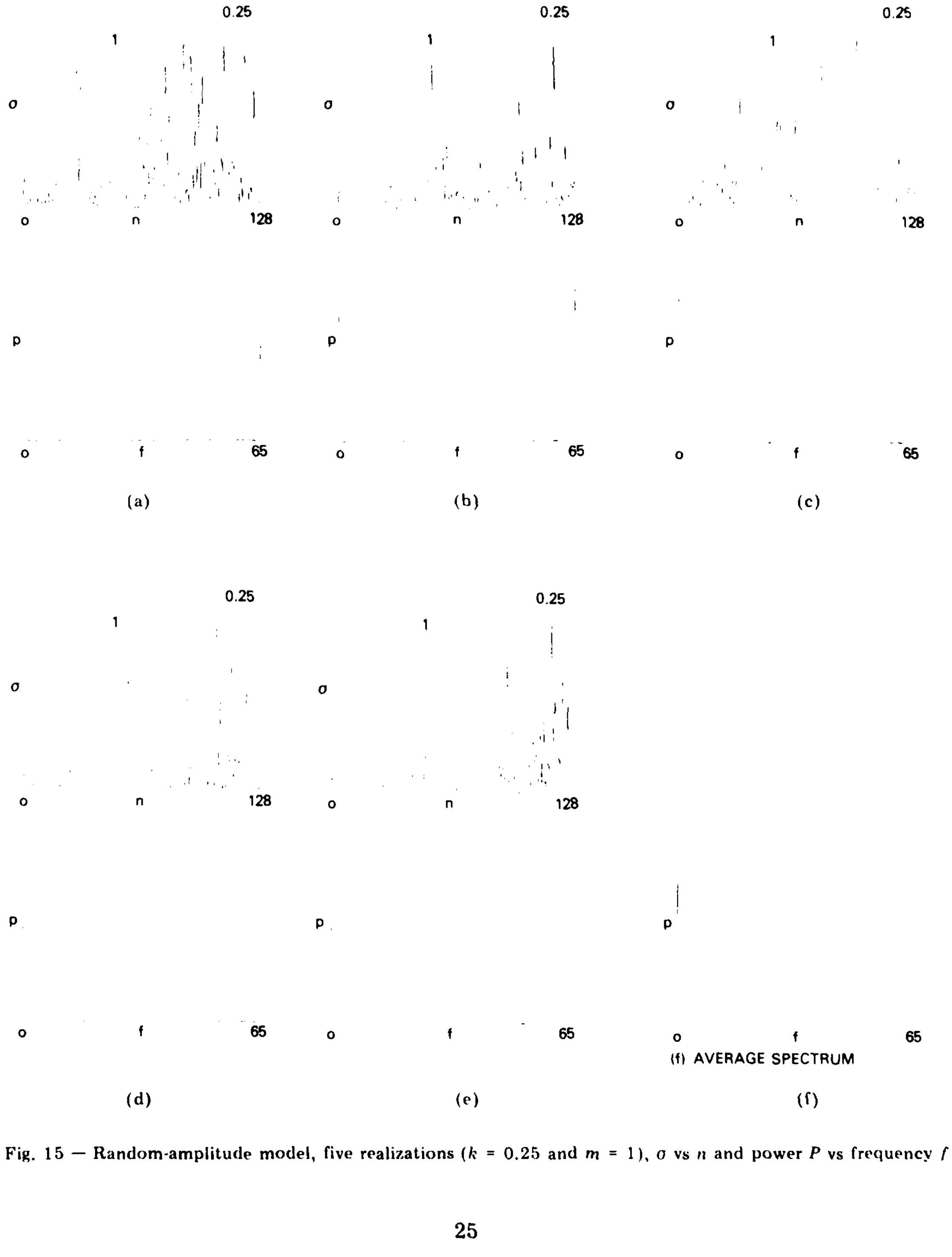

(a) (b) (c)

(d) (e) (f)

Fig. 15 — Random-amplitude model, five realizations (k = 0.25 and m = 1), σ vs n and power P vs frequency f

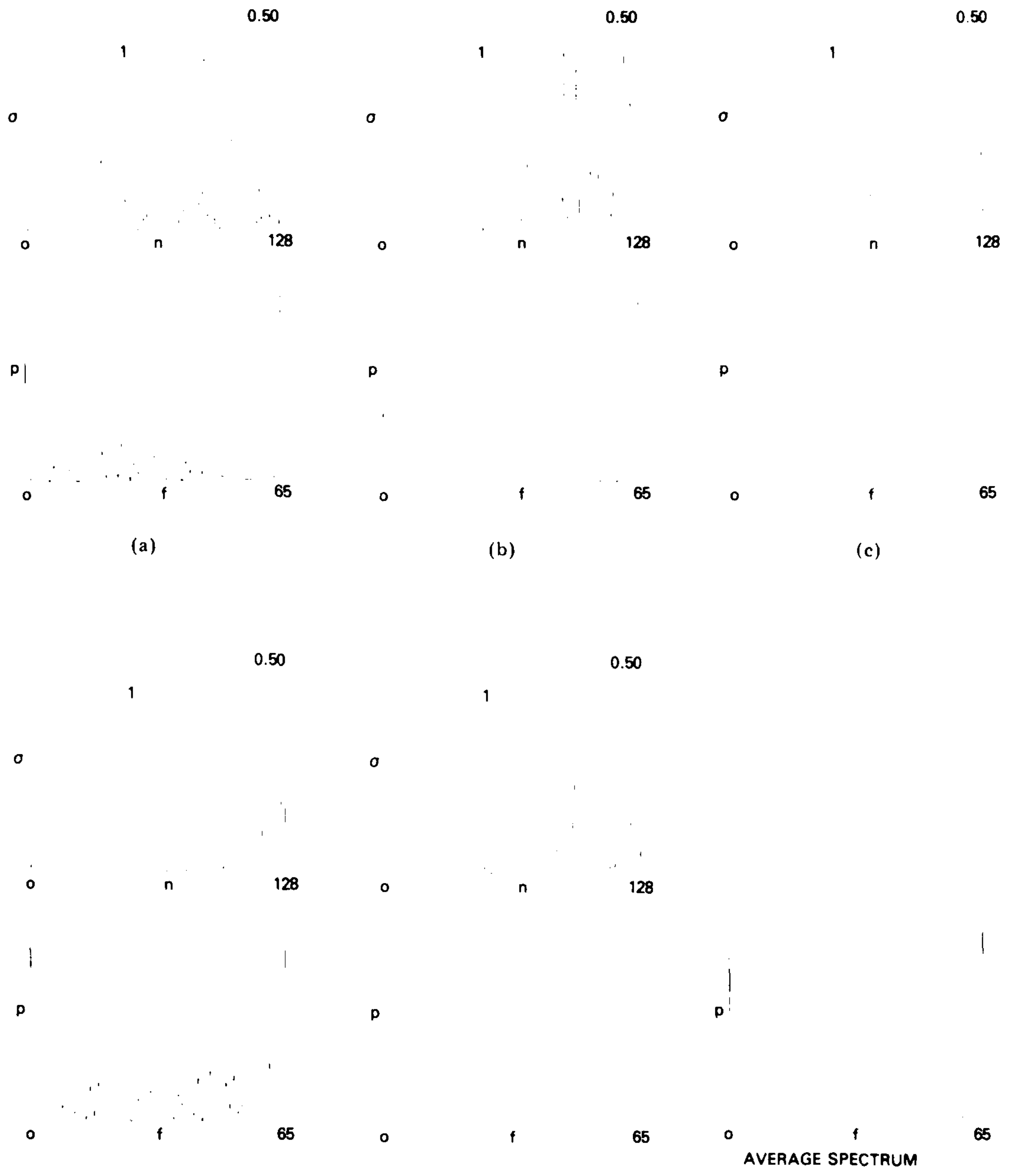

(a) (b) (c)

(d) (e) (f)

Fig. 16 — Random-amplitude model, five realizations (k = 0.5 and m = 1), σ vs n and power P vs frequency f

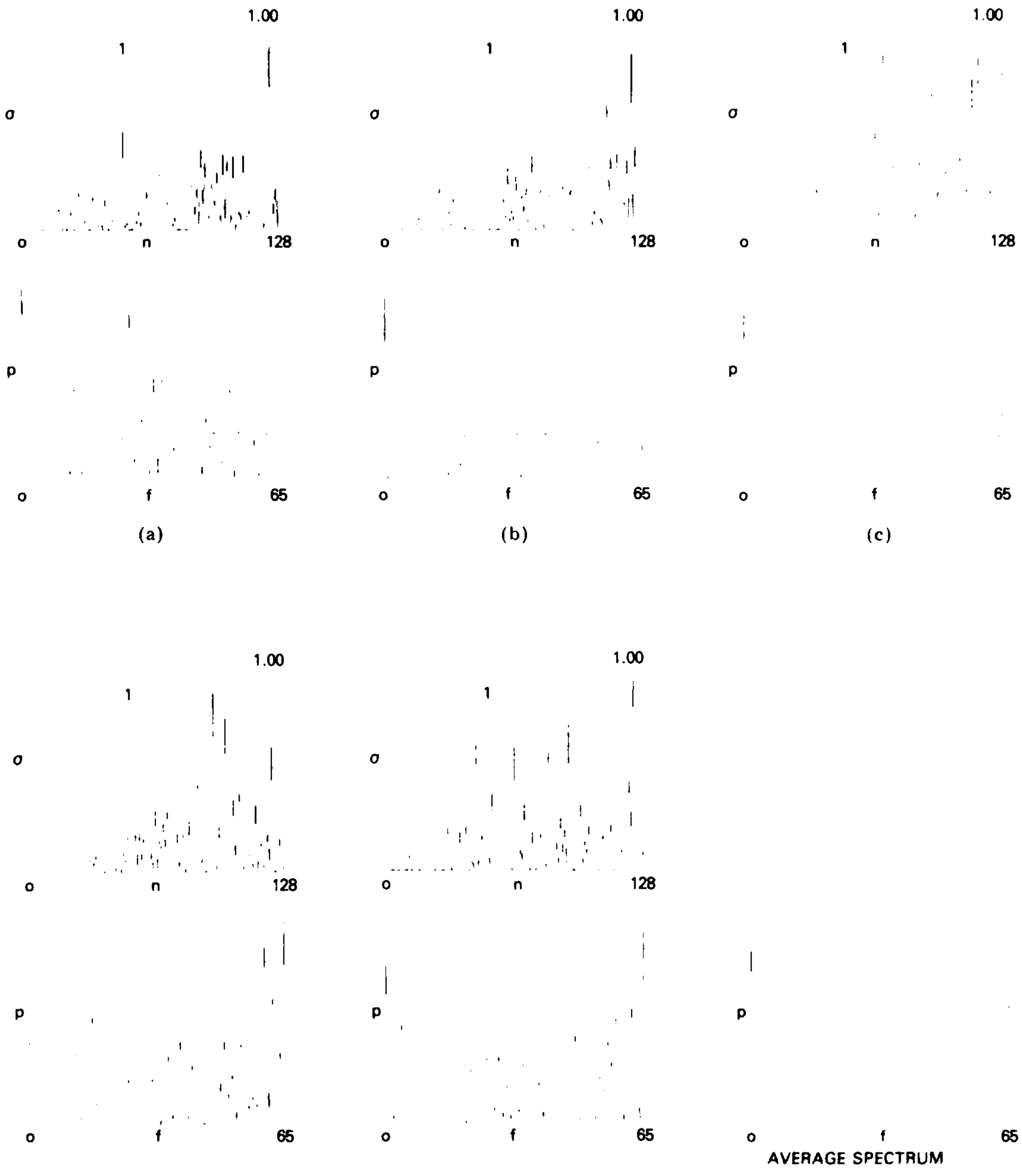

(a) (b) (c)

(d) (e) (f)

Fig. 17 — Random-amplitude model, five realizations (k = 1 and m = 1), σ vs n and power P vs frequency f

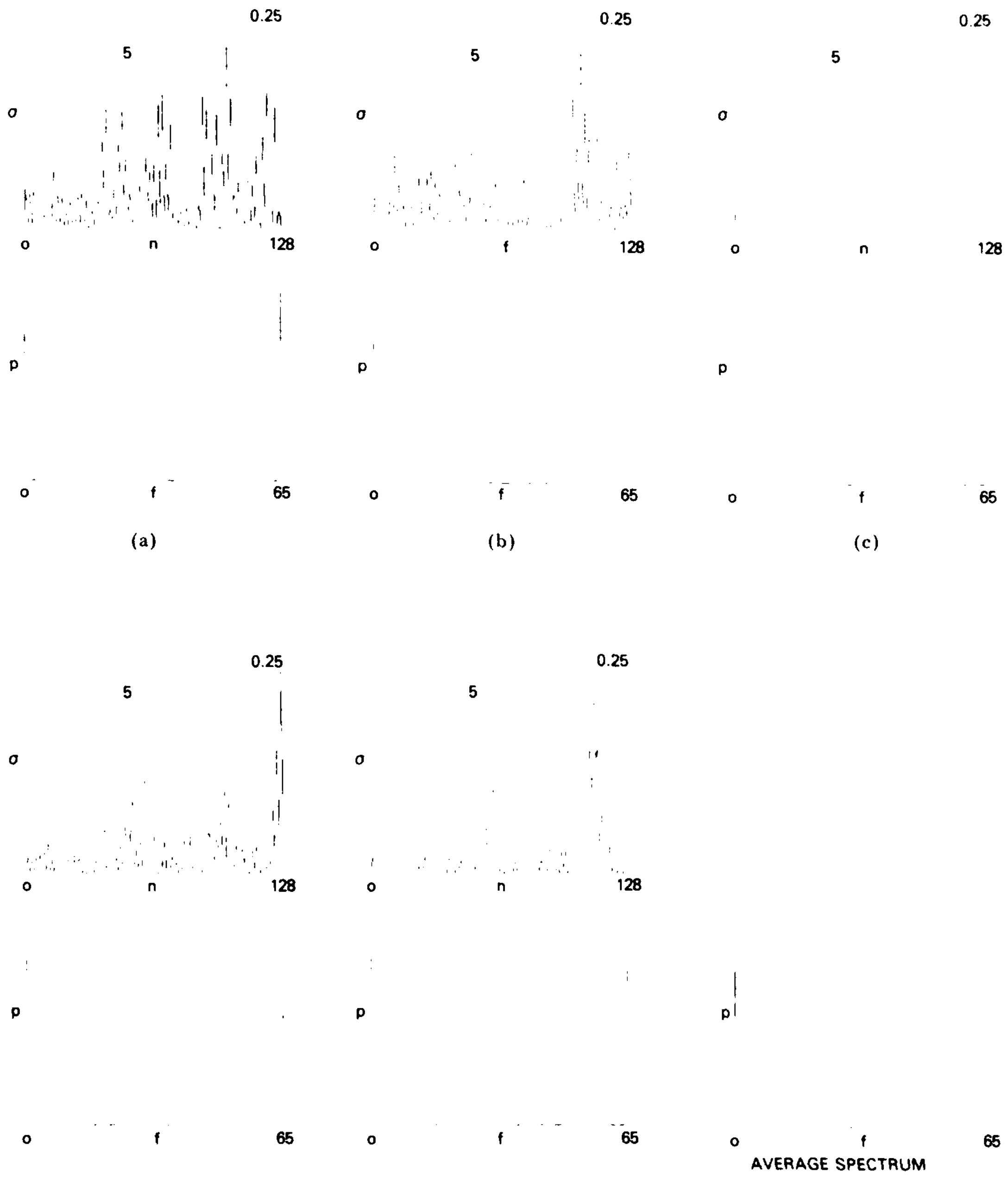

(a) (b) (c)

(d) (e) (f)

Fig. 18 — Random-amplitude model, five realizations (k = 0.25 and m = 5), σ vs n and power P vs frequency f

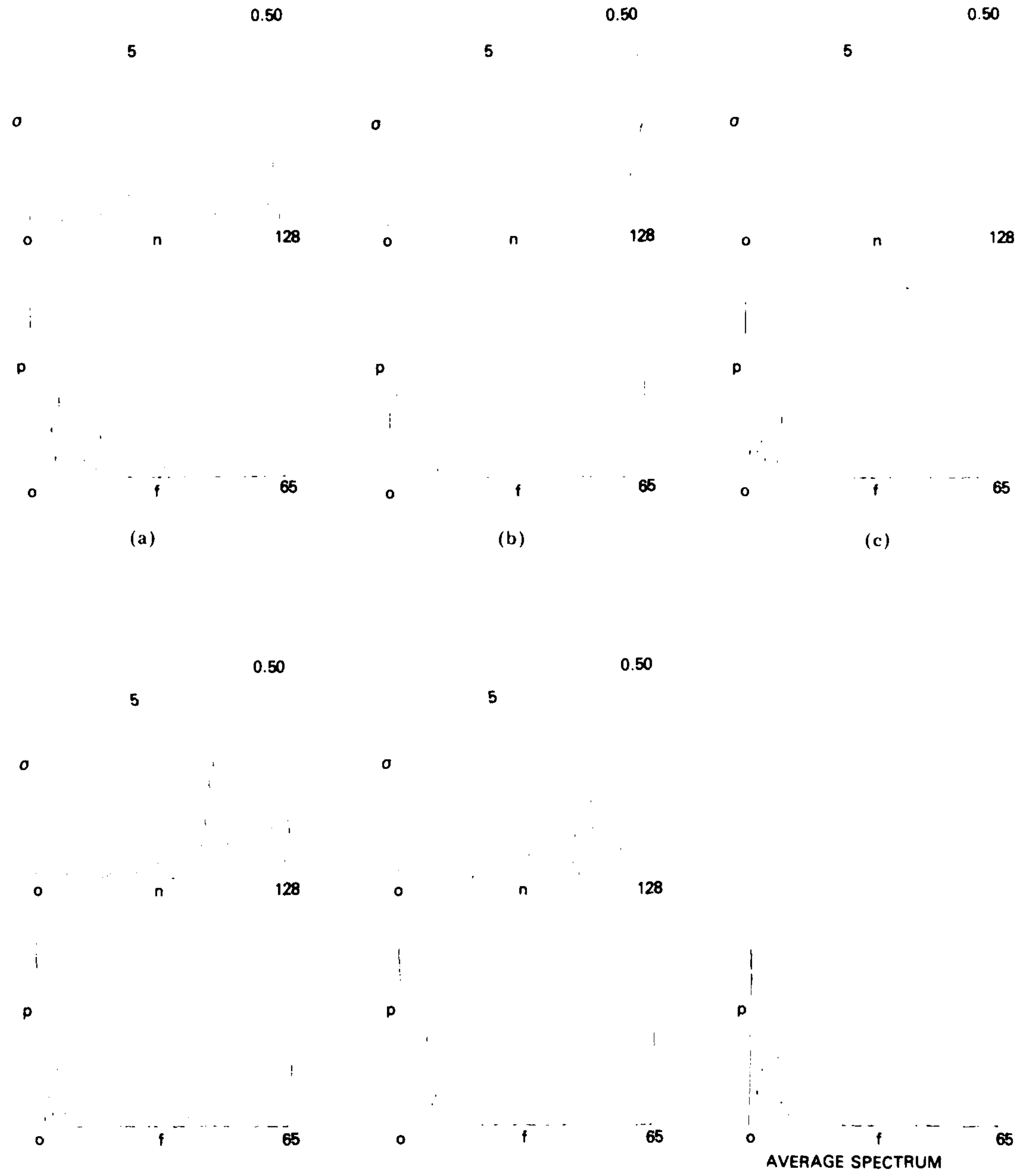

(a) (b) (c)

(d) (e) (f)

Fig. 19 — Random-amplitude model, five realizations (k = 0.5 and m = 5), σ vs n and power P vs frequency f

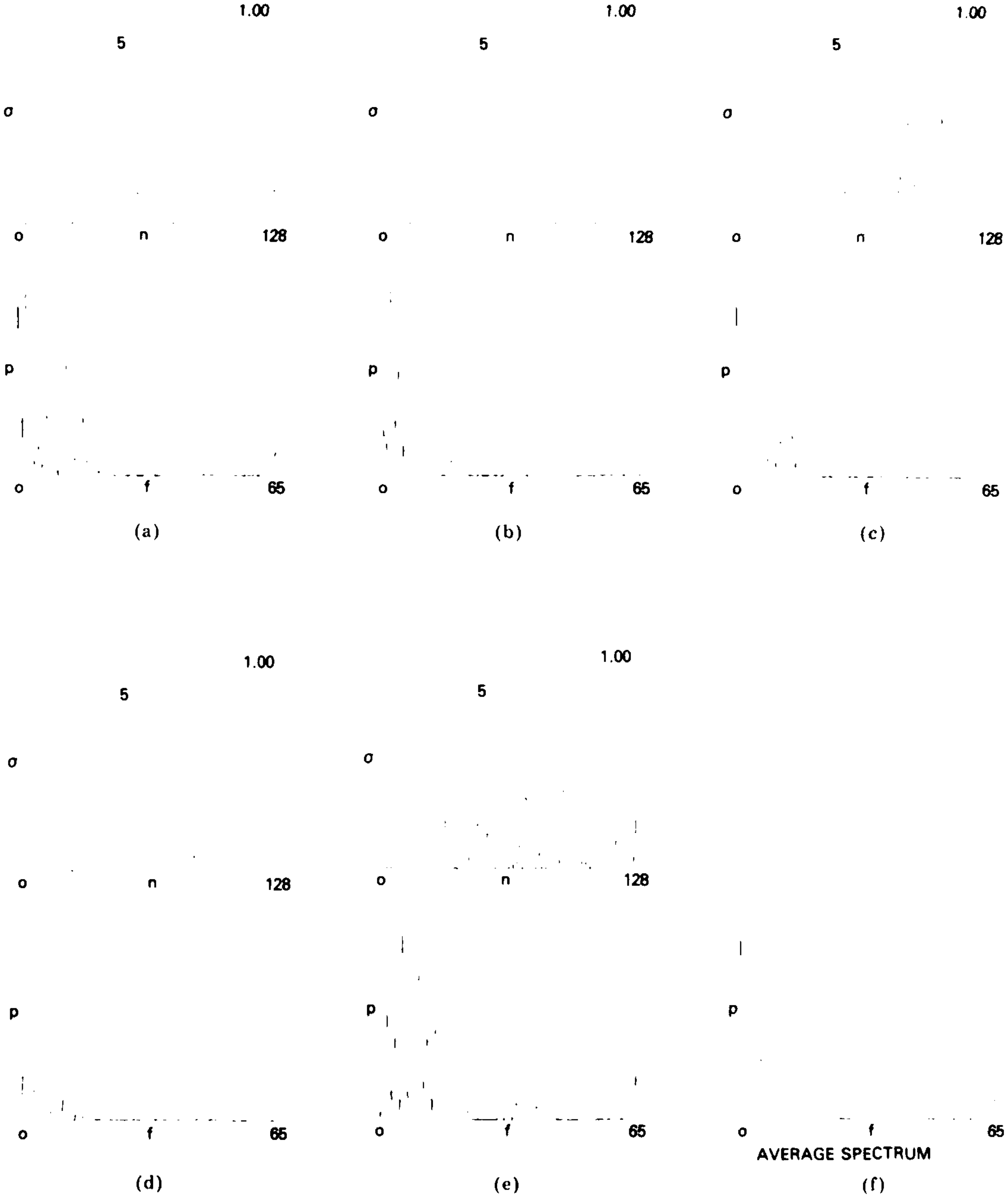

(a) (b) (c)

(d) (e) (f)

Fig. 20 — Random-amplitude model, five realizations (k = 1 and m = 5), σ vs n and power P vs frequency f

Figures 21 through 23 and 24 through 26 illustrate the results of this model with k = 0.25 and 0.5, and 1, and with m = 1 and 5. A comparison of these results with those from the random-amplitude-only model reveals very little difference in character. However, the DC component of the spectra of the m = 1 data appears to be lower in the random-amplitude and random-phase data.

It should be noted that scatterer separations of greater than $\lambda/4$ could have been used in all these models with no significant changes. However, separations of less than $\lambda/4$ would have correlated the surface and made every zone nearly equal in magnitude with a phase center in the center of the zone.

It should also be noted that these models can be used to explain the small-wave Boca Raton data obtained in the absence of whitecaps.

DEBRIS CHARACTERISTICS

The radar echoing characteristics of rigid debris floating on the sea surface were studied both theoretically and experimentally. Oil drums, logs, and aluminum-covered plastic gallon milk bottles were considered and measured.

A comparison of the echoing characteristics of solid debris and the sea surface revealed that returns from debris floating on the sea had much lower frequency-amplitude modulation than sea return. Figure 27 is typical of the data obtained. This figure is the measured (vertically polarized) echo signal from an anchored plastic gallon milk bottle covered with aluminum foil. The gated stretched video was recorded on a visicorder. The low-frequency modulation was produced by 2-ft (0.6 m) waves swinging the bottle on its tether and by interference between the bottle and its image in the sea surface. This piece of data was taken in the absence of a whitecap in the resolution cell. Note that large returns at 8.6 and 9.2 GHz were received at different times. This indicated the aforementioned target image interference phenomena.

Figure 28 is equivalent data taken with the radar polarized horizontally. A small whitecap was in the resolution cell in the left hand portion of this recording and added relatively high frequency modulation components to the bottle return on 8.6 GHz.

Figures 29 and 30 show sea return data from a breaking wave on the two different polarizations for comparison purposes. Note the large percentage of high-frequency amplitude modulation on the sea return.

Calculation revealed that a 3.33-m-long log would have to be seen near broadside rotating at 0.5 rad/s about a vertical axis normal to its long axis in order to produce modulation frequencies near those characteristic of sea return. It is obvious that such a condition could not exist for any extended period of time. This, coupled with the observed fact that whitecaps are very improbable in any given resolution cell, provided the concept necessary for design of an effective debris-avoidance radar.

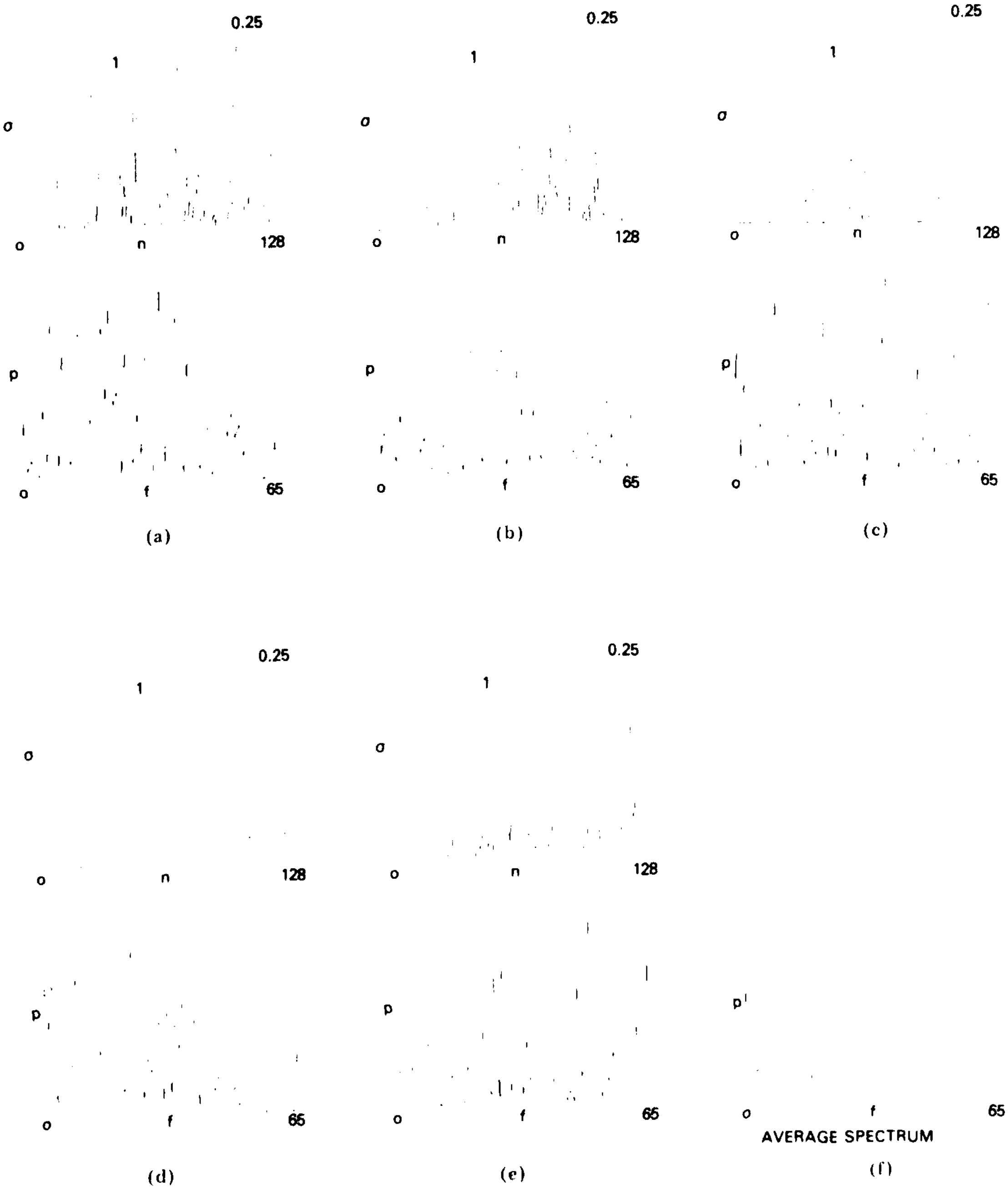

(a) (b) (c)

(d) (e) (f)

Fig. 21 — Random-amplitude and phase model (k = 0.25 and m = 1), σ vs n and power P vs frequency f

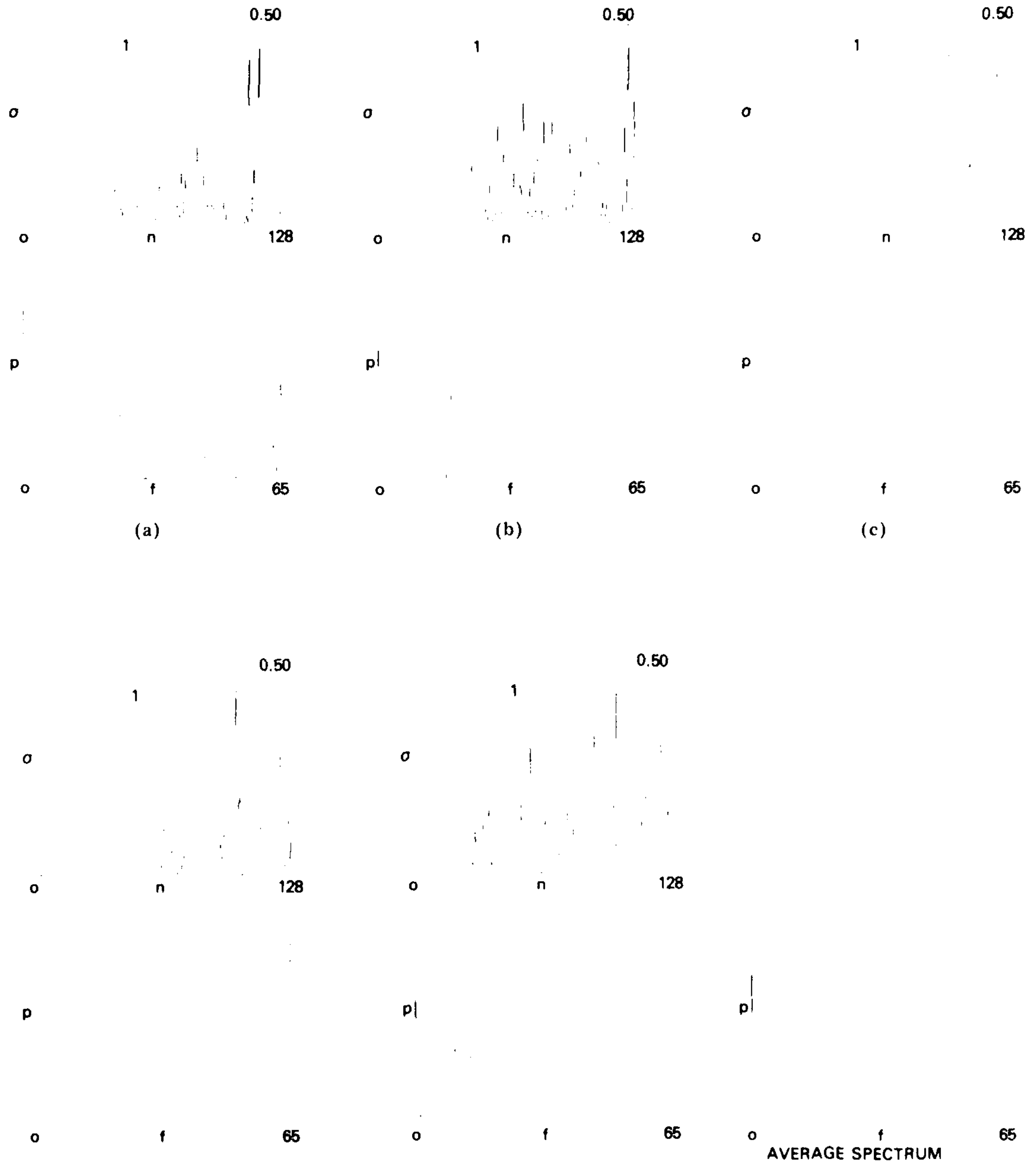

(a) (b) (c)

(d) (e) (f)

Fig. 22 — Random-amplitude and phase model (k = 0.5 and m = 1), σ vs n and power P vs frequency f

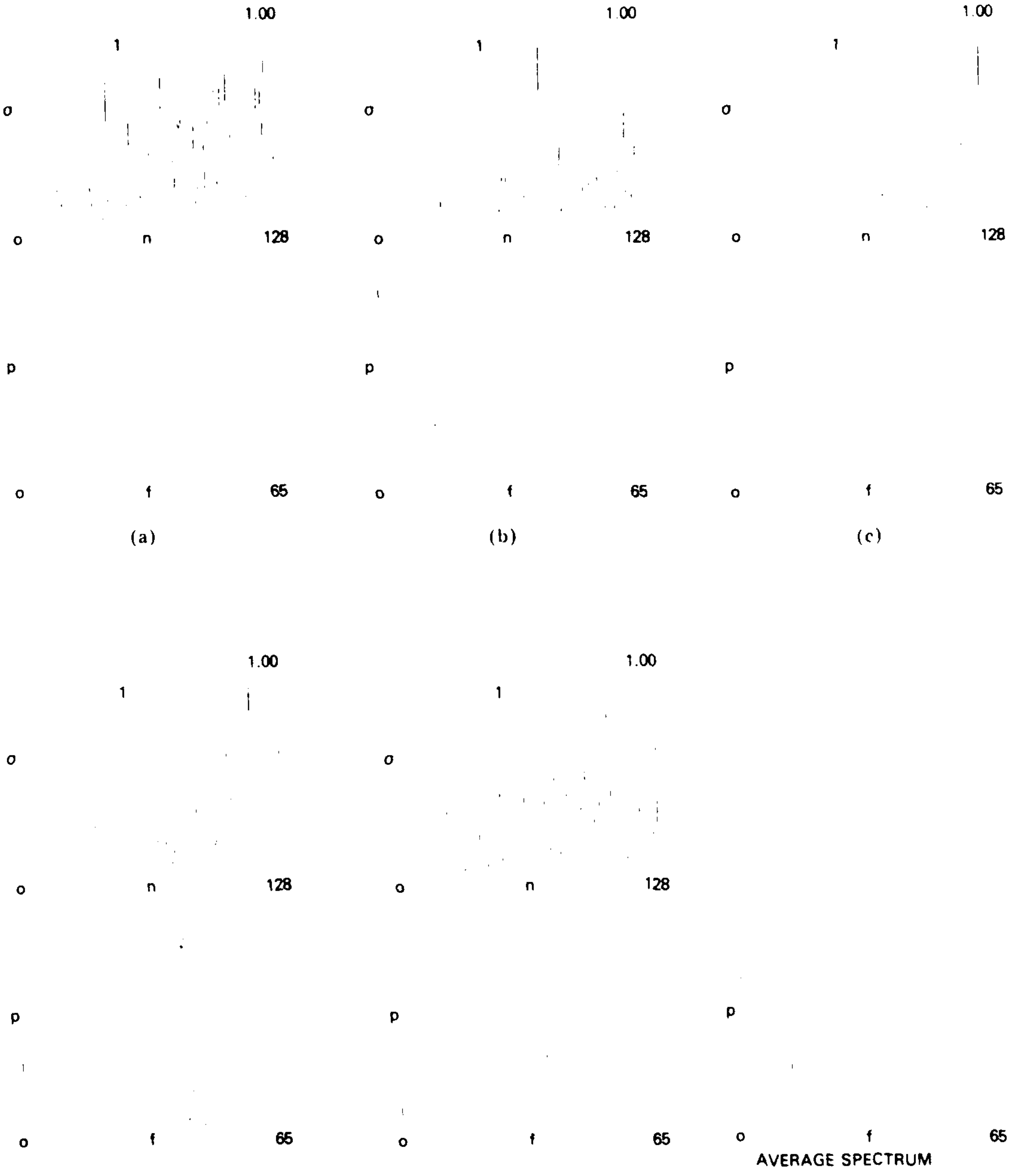

(a) (b) (c)

(d) (e) (f)

Fig. 2[illegible] — Random-amplitude and phase model (k = 1 and m = 1), σ vs n and power P vs frequency f

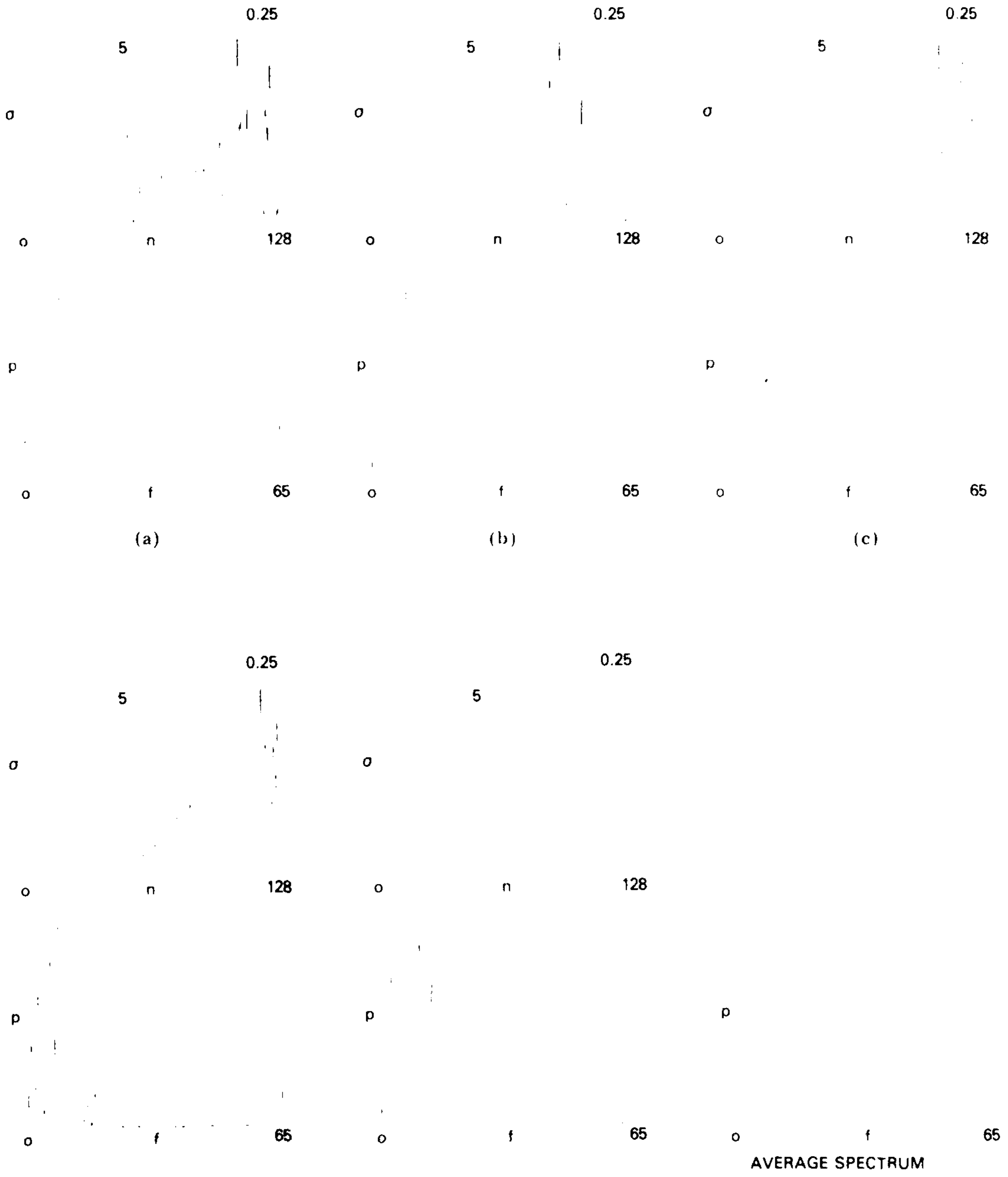

Fig. 24 — Random-amplitude and phase model (k = 0.25 and m = 5), σ vs n and power P vs frequency f

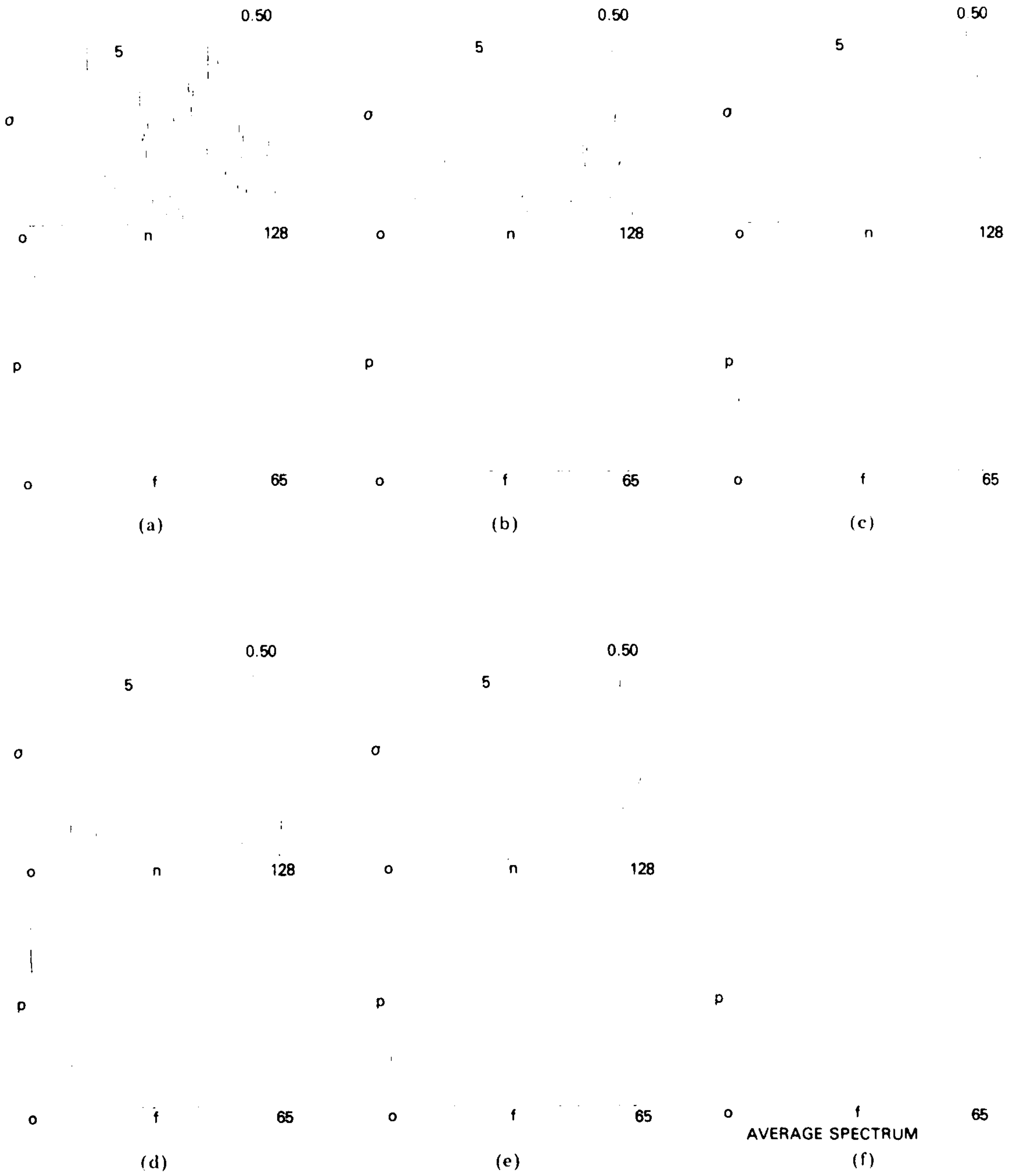

Fig. 25 — Random-amplitude and phase model (λ = 0.5 and m = 5), σ vs n and power P vs frequency f

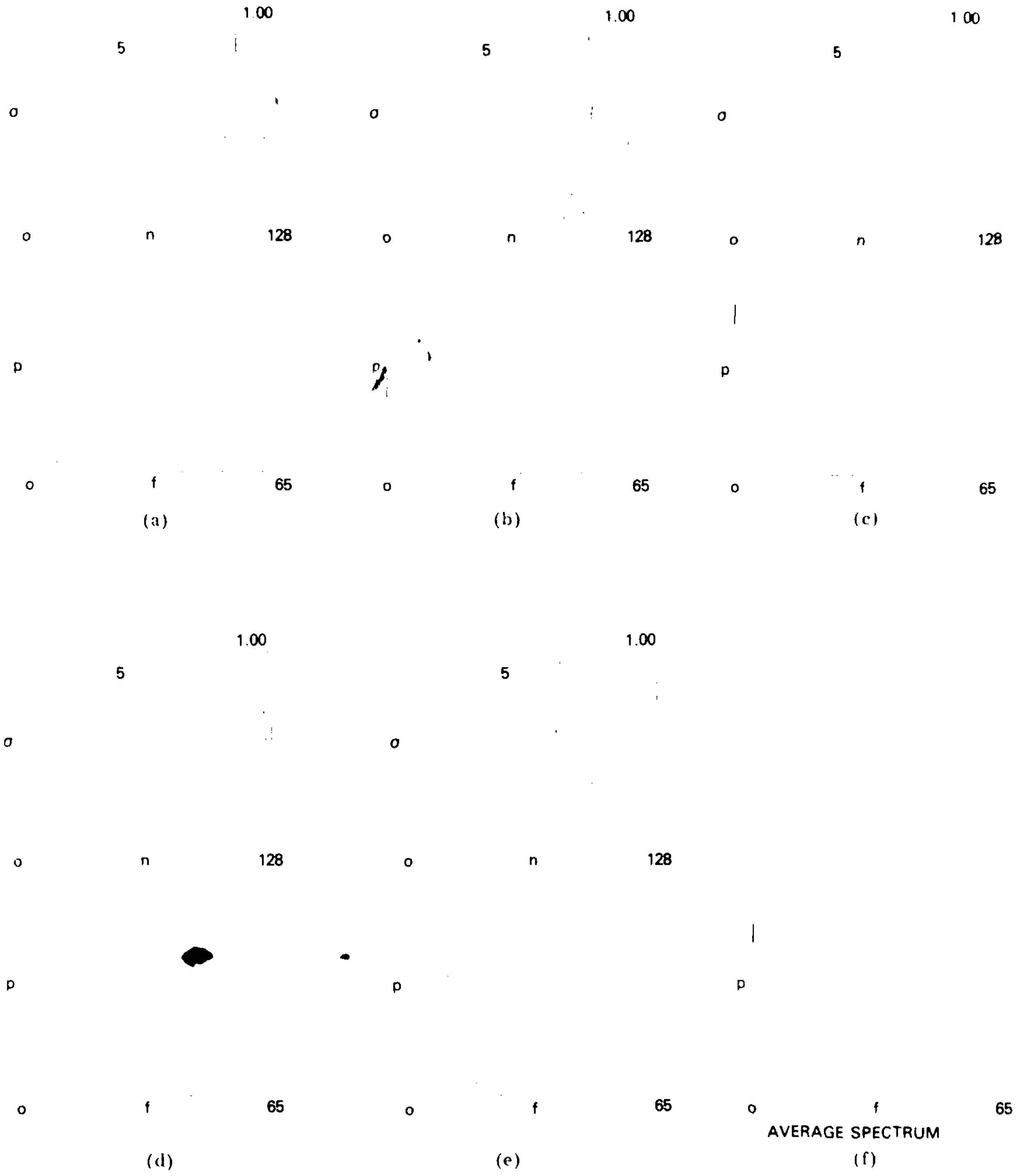

Fig. 26 -- Random-amplitude and phase model (k = 1 and m = 5), σ vs n and power P vs frequency f

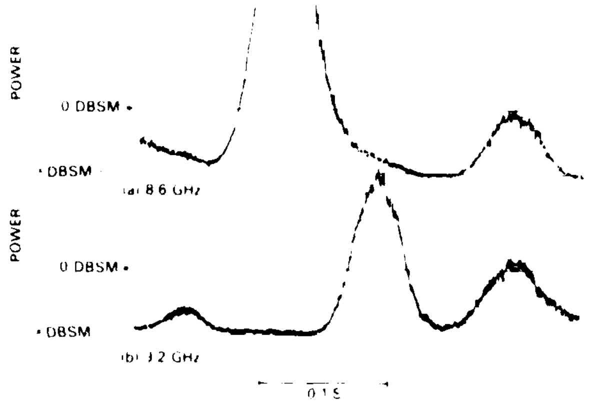

Fig. 27 — Vertically polarized return from foil-covered plastic bottle

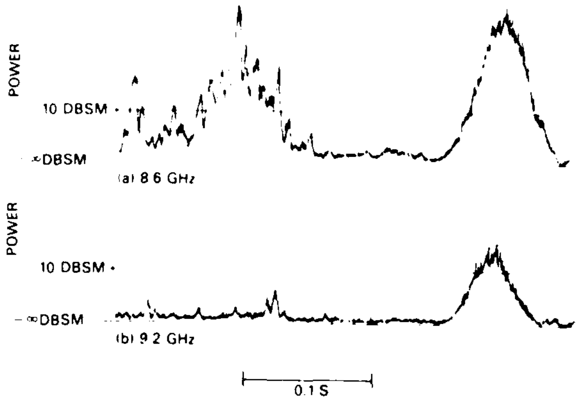

Fig. 28 — Horizontally polarized return from foil-covered plastic bottle

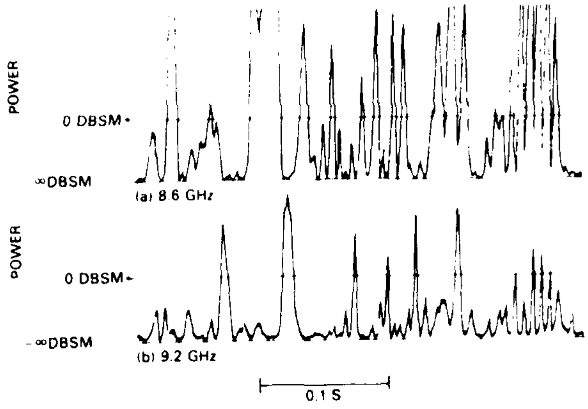

Fig. 29 — Vertically polarized return from wave

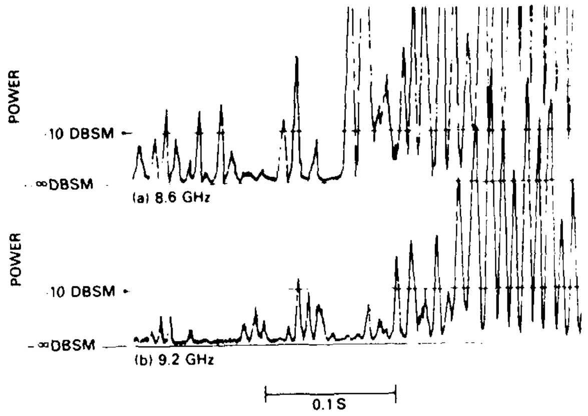

Fig. 30 — Horizontally polarized return from wave

DEBRIS-AVOIDANCE RADAR CONCEPT

The difference in the amplitude modulation characteristic of rigid floating debris and sea return suggests that percentage modulation vs time might be used as a discriminant to suppress sea return. Figure 31 illustrates one way in which such a discriminant might be instrumented. The radar return signals are delayed by integral multiples of the transmitted pulse repetition interval in a tapped delay line similar to those used in moving target indicators (MTI). The outputs of the taps are subtracted from each other as indicated to detect high-frequency, large-percentage amplitude modulation on echoes in any given range resolution cell. If such modulation is detected, the output from one or more of the subtractors will exceed a preset threshold and inhibit a gate to block passage of that video to a display. Since sea return fluctuates by more than 6 dB in less than 20 ms and debris echoes remain constant for much longer intervals, this instrumentation will block all sea return video and pass debris video.

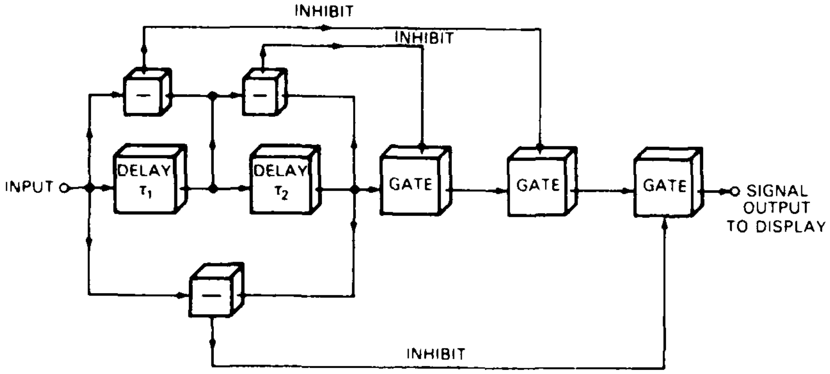

Fig. 31 — Proposed sea return suppressor

This instrumentation should not materially reduce the probability of detection of debris, since sea return is expected only about 1% of the time in any given range cell. Thus, when sea return and debris return come from the same cell and that cell is blocked, the blockage will correspond to a mere 1% reduction in viewing time.

To employ the percentage-modulation-vs-time discriminant, the radar must dwell on the same region long enough to suppress sea return and ensure debris detection. Such long dwells can be provided by employing a roll- and pitch-stabilized antenna with multiple azimuth beams filling a 10° or 20° sector looking forward in the direction of the ship motion. The beams can be spoiled downward to permit observation of the sea surface near the ship but should be limited in width above the horizon to reduce weather clutter.

The azimuth beamwidth and range resolution should be designed to ensure low probability of including a whitecap in any given resolution cell. A study of the measurements made to date reveals that 1° beamwidths and 20-ns pulse widths should be adequate for ranges between 1.6 and 4.8 km.

Frequency diversity in the form of simultaneous short pulses on different carrier frequencies would improve the probability of detecting debris by filling in the elevation lobing nulls produced by target and image interference.

PLANS FOR THE FUTURE

Plans for the future include the following:

1. Bistatic measurements of sea scatter as a function of polarization and frequency will be made, to test the long-wire scattering model.

2. Monostatic sea return measurements using short pulses on a 3-GHz carrier will be made, to verify the linkage between echo autocorrelation time and the time required to add or subtract one $\lambda/4$ zone to a whitecap.

3. Three extra sample-and-hold circuits will be added on each X-band frequency, and four contiguous range cells will be gated. A target will be anchored in one of the gated range cells, and target and/or sea returns will be recorded on magnetic tape from each stretcher. These data will then be processed to determine the optimum thresholds for suppressing sea return and detecting debris.

4. A multibeam radar will be instrumented and fitted with the proposed data processor and will be tested at sea.

SUMMARY AND CONCLUSIONS

The experimental measurement program revealed that high-resolution X-band radar echoes from a disturbed sea surface are very improbable in any given resolution cell and that when they occur they are always amplitude modulated with a high modulation index and have a lifetime on the order of 1 s. The modulation function was observed to have autocorrelation times of 10 ms or less. Echoes from rigid objects floating on the disturbed sea surface were found to have much longer autocorrelation times than echoes from the sea. This difference was used in designing a signal processor that would suppress sea echoes and permit detection of debris echoes.

Theoretical models of the sea scattering phenomena were developed to explain the temporal and spatial characteristics of sea return. In addition, the effect of radar polarization on sea returns was considered and an explanation for its effect was suggested. The theoretical work aided in justifying the proposed debris-avoidance radar concept that was derived from the experimental data.

The principal conclusion that can be drawn on the basis of this effort is that it should be possible to design an effective debris-avoidance radar for high-speed ships. On the basis of this conclusion, continuation of the program is recommended.

REFERENCES

1. Nathanson, F.E., *Radar Design Principles*, p. 228-238, McGraw-Hill, New York, 1969.
2. Jasik, H., ed., *Antenna Engineering Handbook*, p. 4-1 to 4-7, McGraw-Hill, New York, 1961.
3. Wolf, E.A., *Antenna Analysis*, p. 372-379, John Wiley and Sons, Inc., New York, 1966.
4. Skolnik, M.I., *Introduction to Radar Systems*, p. 42, McGraw-Hill, New York, 1962.
5. Hicks, B.L., Knable, N., Kovaly, J.J., Newell, G.S., Ruina, J.P., and Sherwin, C.W., "The Spectrum of X-Band Radiation Backscattered from the Sea Surface," *J. Geophys. Res.* 65 (3), 825 (Mar. 1960).